Doctoral Thesis

Dynamic Self-Assembly and 3D Fluidic Trap in Rotating Fluids

Taehoon Lee

Department of Chemistry

Graduate School of UNIST

2020

Dynamic Self-Assembly and 3D Fluidic Trap in Rotating Fluids

Taehoon Lee

Department of Chemistry

Graduate School of UNIST

Dynamic Self-Assembly and 3D Fluidic Trap in Rotating Fluids

A thesis/dissertation
submitted to the Graduate School of UNIST
in partial fulfillment of the
requirements for the degree of
Doctor of Philosophy

Taehoon Lee

12/27/2019
Approved by

_____

Advisor
Bartosz A. Grzybowski

Dynamic Self-Assembly and 3D Fluidic Trap in Rotating Fluids

Taehoon Lee

This certifies that the thesis/dissertation of Taehoon Lee is approved.

12/27/2019

signature

_____

Advisor: Bartosz A. Grzybowski

signature

_____

typed name: Steve Granick

signature

_____

typed name: Oh-Hoon Kwon

signature

_____

typed name: Hyuk Kyu Pak

signature

_____

typed name: Yoon-Kyoung Cho;

Abstract

This thesis describes a dynamical system enabling the formation of ordered structures and particle trapping established in non-inertial frame of reference. Lighter particles suspended in a denser rotating fluid filling a cylindrical tube can be localized on the axis of rotation by the axis-symmetric centripetal force. Such particles can self-assemble into ordered tubular structures with mild rotational accelerations and the types of the resulting packings are dependent on the particle's concentration. We demonstrated various tubular structures of symmetries ranging from simple helix (C_1) to double helix, D_{2d}, and D_{3d}. Using the fact that there exists a transient flow along the axis when the rotational rates are abruptly accelerated or decelerated, the structures can interconvert into each other by quickly changing the rotational rates. In addition, the chirality for the chiral structures can be selective when the system's orientation is adjusted with respect to gravity. We also report unprecedented binary tubular structures by using two types of particles differing in density and/or size. On the other hand, when the particles confined in the axis-symmetric potential can experience confinements along the axis of rotation, the particles can be trapped and assemble into 3D ordered structures. We realized the axial confinement with disks which are fitted inside the tube and rotate slower than the surrounding fluids by the external magnetic field (the so-called eddy current brake), giving rise to vortices. The strength of the axial confinement by the vortices is inversely proportional to the speed of the disk relative to the fluids. When such two disks are placed near each of the both ends of the tube, the particles can be trapped between the disks if the rotational rates of the tube and the disks are properly adjusted. Depending on the relative strengths of the radial and axial confinements, the trapped particles can exhibit the orbiting trajectory, linear assembly, or ordered packing. Similarly, particle clusters can have geometries of prolate, oblate or spherical symmetric shapes. We showed various types of ordered packings using a few spherical particles and demonstrated various dynamic assemblies of cages and interlocked architectures with non-spherical particles as well as jammed colloidal monolith. As we obtained unusual binary tubular structures by using different types of particles, certain combinations of the particles can exhibit structural selectivity for polymorphic system. Last but not least, our system is found to undergo interesting transition behavior such as Hopf bifurcation and others including two limit cycles.

Contents

List of Figures

Chapter1. Introduction

Dynamic self-assembly of tubular structure

Before the study of dynamic self-assembly, static assembly is preferentially considered and many fascinating examples – some of which have found its application to industry and some increased our understanding on naturally occurring phenomena – have been demonstrated. Despite such successful demonstrations and findings, the study of self-assembly cannot be completed without taking account of assembling system in non-equilibrium state. Nature, which provides typical and important examples of static self-assembly and is a motivation of this field of study, also consists of many living systems (biological assemblies) that reside in continuously changing environment and are maintained through dynamical processes. Although ascending attentions have been made on dynamic self-assembly and there have been some progresses since 1990's, it is still at an early stage of its development, in particular, for microscopic systems due to the lack of our knowledge dealing with (covering) non-equilibrium state at microscopic scale.

Dynamic self-assembling systems, those that function in out-of-equilibrium and require continuous energy supply to sustain the formed structure (*1*), are ubiquitous in nature and have shown that it can also be artificially created in unnatural system. Examples include dendritic growth in solidifying alloys (*2*), quasi-crystalline pattern in interfacial waves of fluids (*3*), and dynamic structures of micro- and milli-meter sized particles in varying magnetic field (*4*,*5*). Nature of residing away from an equilibrium allows the dynamical system to produce complex spatiotemporal patterns or structures that are not usually obtainable from static self-assembling system. Despite this high potential of creating diverse structures, dynamic system exhibiting highly ordered structure or rich phase behavior has not been extensively exploited except for a few exceptions (*6*), and, in particular, design of multicomponent dynamic self-assembling system is highly challenging.

We chose a rotating frame of reference as a test bed (platform) for the exploration of dynamic self-assembly. In our study, the non-inertial frame of reference is combined with buoyancy such that centrifugal force can localize lighter particles immersed in a denser rotating fluid onto the axis of rotation. Since we used cylindrical tube to accommodate the particles and fluid (the components), the assemblies formed by those particles result in tubular structure. Starting from a simple chain-like structure – all the particles fit into a single line on the axis of rotation – double and triple helical structures and those having symmetries of D_{2d} and D_{3d} have resulted (form) as the number of particle increases. In comparison to previous studies of the tubular structure, following characteristics feature in our assembling system. First, the strength of particle confinement is determined by the fluid's rate of rotation. This property enables different structures to be interconverted in a process of acceleration or deceleration of the fluid (by accelerating or decelerating the fluid). Second, for the

helical structures, chirality can be selectively chosen to a certain extent by adjusting the orientation of the fluid's axis of rotation with respect to gravity.

3D fluidic trap and Hopf bifurcation

Particle trapping has been successfully explored in various studies such as Brownian motion of a single particle (*7*), Bose-Einstein condensation (*8*), and mechanical properties of biomolecules and cells (*9*,*10*) and recent progress on multiple-particle manipulation can achieve plane-by-plane atom assembly (*11*). Much efforts have been made to develop robust trapping methods since the pioneering work of Ashkin in 1970s (*12*,*13*). Particles can be trapped and manipulated either by gradient force exerted by externally applied fields such as optical (*14*), magnetic (*15*), electronic (*16*), and acoustic (*17*) fields or by hydrodynamic effects in a microfluidic device (*18*,*19*). On the other hand, to overcome the limit of one trapping method, a hybrid (combined) technique has been frequently adopted (*20*,*21*).

Helical vortex is frequently encountered in nature or everyday life (e.g., a whirlpool in a river, a tornado, and draining water in a bathtub) and also arises in many engineering designs such as a delta wing (*22*), a turbine rotor (*23*), and a building roof (*24*). Consequently, there have been continuous efforts to understand the properties (e.g., stability (*25*), helicity (*26*), motion (*27*), and velocity field (*28*)) of the helical vortex. Although it is not difficult to find some applications in which the vortices are harnessed to separate a solid-liquid mixture (*29*) and enhance heat transfer (*30*) and mixing in a combustion system (*31*), the intricacies of the vortex dynamics make it difficult to be exploited in a broad area of science and technology.

In this work, we present 3D fluidic trapping which utilizes the helical vortices in combination with the centripetal acceleration to create non-contact mode trapping of particles. This work was motivated from the question whether it is possible to create 3D structure in our rotating system which demonstrated the quasi-1D dynamic self-assembly. In order to achieve the conversion from quasi-1D to 3D, the radially-confined assembly should experience another confinement in lateral direction. The additional confinement was realized by utilizing a pair of collinear vortices. Two aluminum disks which are fitted inside and positioned near both ends of the tube are dragged by external magnetic field, and subsequently rotate slower than the fluid. The difference in rotation rates of the disks and fluid gives rise to vortices, effectively pushing and confining particles between (particles towards the middle of) the two vortices. When this lateral confinement is coupled together with the centrifugal force, there can exist a region in which particles can be stably trapped under the properly controlled condition – viscosity of the fluid, rotation rate, density difference between the particle and fluid, etc. With a few numbers of spherical particles, we demonstrate simple molecular geometries such as tetrahedral, square pyramidal and octahedral shapes and so on. Moreover, using the facts that

confining potential of our system is harmonic with respect to radial position and the strength of the confinement can be regulated, we show the selective formation in a polymorphic cluster and atypical dynamic process of structure transformation, respectively. Our dynamic system which enables 3D fluidic trap and a variety of 3D assemblies therein has following 4 essential properties: i) comparing to other conventional trapping methods, the trap has a large basin of attraction and high trapping strength; ii) diverse geometries of the trap (or diverse types of packings) are achievable due to adjustable confining forces (in radial and axial directions) controlled by fluid's rotation rate and intensity of magnetic field; iii) the trapping occurs due to a combination of hydrodynamic and inertial (centripetal) forces; iv) the system shows supercritical Hopf bifurcation.

1.1 Thesis structure

The thesis is comprised of two researches (i.e., tubular structure formation and 3D fluidic trap) as described in the Introduction. The following two chapters delineate each of the two studies: tubular structure formation is depicted in **Chapter 2** and 3D fluidic trap in **Chapter 3**. In fact, these research outcomes are already published in Wiley in 2017 and 2019, respectively. Since I believe that the published form itself describes these studies in concise and precise manner, and also includes most of the essential part of outcomes, I decided to reuse the article – including supporting information – as intact as possible in descriptions of the following chapters. Each chapter contains the license for reusing the published paper at the end of the chapter. The supplementary parts that need to be added in this dissertation will be depicted in the following sections in this chapter with appropriate subtitles.

1.2 Dynamic self-assembly of tubular structure

Experimental system

Rotational motion of cylindrical tube was easily obtained by connecting the tube with rotating machine for which we used a commercial lathe (Sherline Products 4100A-DRO). Since the tube has the aspect ratio larger than 5 and rotates at high speed (> 3000 rpm), stable rotation can only be achieved by mounting another end of the tube on a ball bearing which must be precisely aligned with the axis of lathe (see **Figure 1**).

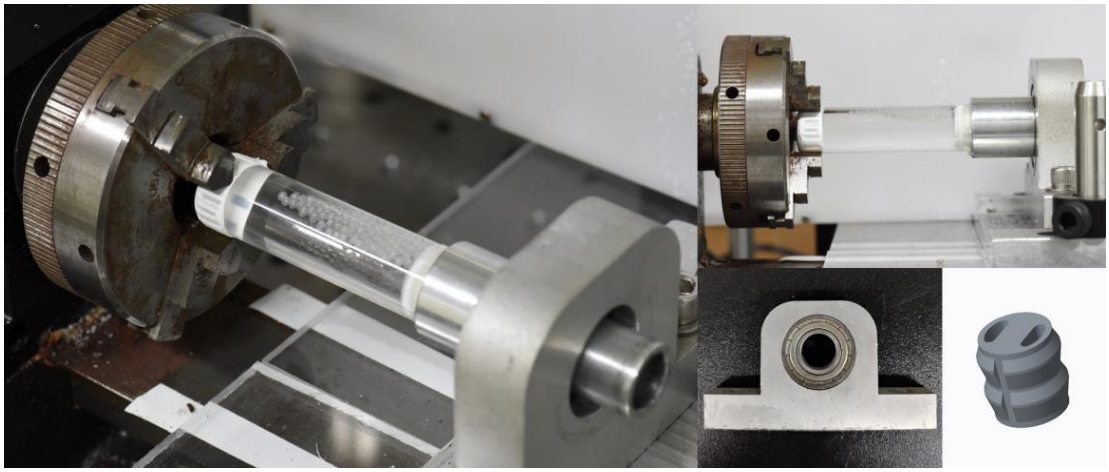

Figure 1. Photo of experimental configuration. Both ends of the tube are mounted on a lathe and a ball bearing in order to obtain stable rotational motion. The ball bearing should be aligned with the axis of the lathe. The ball bearing is inserted into the home-made frame which is free to move on a rail of the lathe. The sealing cap is fabricated vis 3D printing.

Alignment of the two mounting pieces is the most essential part in experiment to obtain a good quality of assembled structure, in particular for microscopic particles. Increasing the moment of inertia of the sample is also frequently used method to remove any vibration during rotation. Another technical issue to be surmounted is to remove air bubbles during the sample preparation. Degassing the fluid under a vacuum, grinding the surface of a sealing cap and adding a surfactant are the steps we took to make an intact sample. Well-designed sealing cap is also important for reliable experiment. The sealing cap should be tightly fitted into the glass tube to endure long-time and high-speed rotation, while it also needs to be soft enough for an insertion into the tube. In addition, we engineered the side of the cap in a stepwise fashion in which bubbles penetrated during rotation can be captured between the peaks. One example of our cap is presented in Figure 1.

Regular dispersion of a few particles in rotating fluids

What led us to the study of structure formation in rotating frame of reference was the observation that a few particles being localized on the axis were evenly distributed by the vortices produced around them. When the rotation of the tube increases from a rest, the particles rotate slower than the surrounding fluids before the system establishes solid-body rotation. Due to the temporal difference of the rotation rates between the particles and the fluids, the vortices can arise around the particles, acting as repulsion between the particles. **Figure 2** shows patterns of particles developed at various rotational rates – the evolution of the pattern formed by particles with the variation of the rotation rate. While there are no long-range interparticle interactions at low ω ($\lesssim$ 400; a and b in the figure), there exists repulsion between the particles – although it is transient – at higher ω ($\gtrsim$ 500; c–f in the figure). The

particles can be evenly distributed due to the repulsive interactions between the particles. This ordered pattern was the motivation for the study of tubular structure formation.

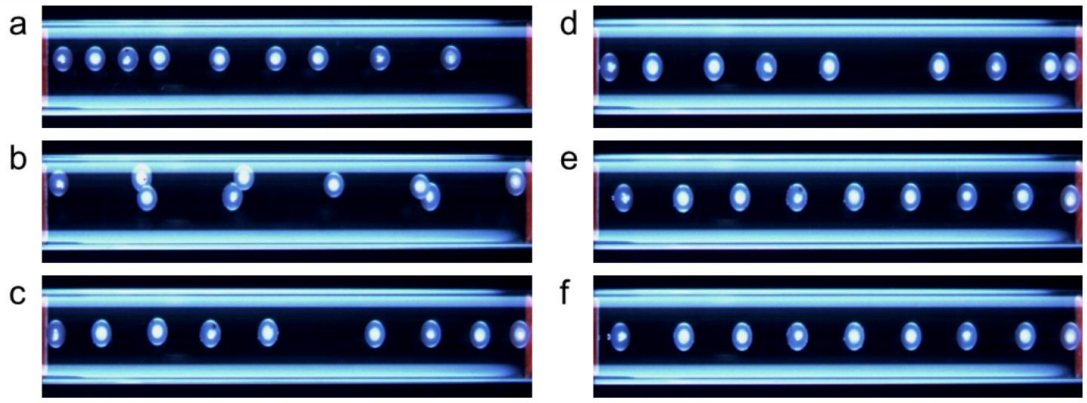

Figure 2. Even distances between the particles in a rotating fluid. a) Particles are simply afloat without any long-range interparticle interaction (ω = 50 rpm). b) Upon increase of the rotation rate (ω = 390 rpm), the particles show a chaotic motion. There exist repulsive interactions between the particles enabling ordered patterns at rotation rates of (c) 770 rpm and (d) 2810 rpm. More perfect ordering can be achieved by decreasing and re-increasing the rotation rates – this is attributed to the transient flows which will be described later. With this approach, more well-ordered patterns were obtained at rotation rates of (e) 860 rpm and (f) 2840 rpm.

Simulation study

We experimentally proved that the parameters crucial for the structure formation were the concentration of the spheres in single component system, and size and number ratios of the components in binary component system. However, there are still many other parameters to control in this system; for example, the hydrodynamic force acting on the sphere is a function of the sphere's volume, densities of the sphere and the liquid, the angular acceleration, and the viscosity of the fluid. To rigorously examine the effect of these parameters on the structure formation, we simulated the packings by means of discrete element method (DEM) and adopted 'velocity Verlet' algorithm to solve Newton's equation of motion. In the simulation, we ignored the rotational motion of the sphere about its axis because the motion is transient and its effect, such as repulsive interactions between the spheres, is negligibly small in a regime of solid body rotation. Moreover, when the particles form a cluster, the rotation of individual particles is highly inhibited by the friction between them. On the other hand, in the simulation we monotonically increased the rotation rate from rest, whereas in experiment we generated the structures by varying the rotation rate back and forth. Despite these simplifications, we reproduced all of the structures that were experimentally observed in single component system (see **Figure 3**). However, the polymorphs in binary component system were not

obtained in the simulation; this indicates that complicated flows induced by varying the rotation rate play an important role for the formation of the polymorphs.

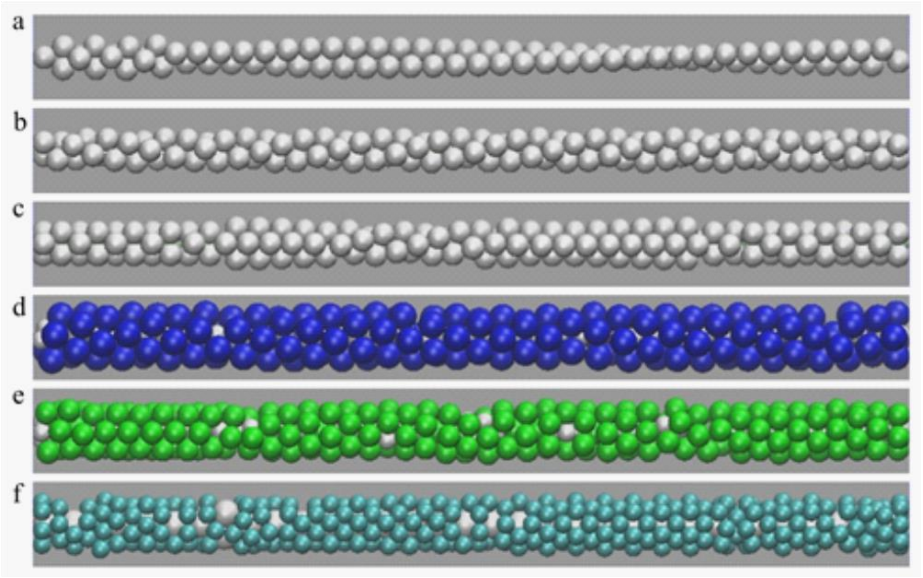

Figure 3. Molecular Dynamic simulation results for a) – c) single component system and d) – f) binary component system. In single component system, the polymorphic nature is reflected; mixed structures of (a) C_1 and D_{2d} symmetries, (b) triple helix and glassy packing, and (c) D_{3d} and D_{2d} symmetries. For binary component system, the structures with rotational symmetries of d) 4-fold, e) 5-fold and f) 6-fold were represented.

Since the hydrodynamic force applying on the sphere is a quadratic function of the rotation rate, we investigated the influence of the rotation rate on crystallization process. It turns out that the crystal exhibited a tendency that it enhanced its degree of ordering with an increasing rotation rate. Our system is also dependent on the rotation rate in such a way that mixed structures, which are frequent observations at mild rotation rates, transformed into a single structure; one of the polymorphs is exclusively dominant at much high rotation rate. These observations clearly indicate the dependence of the crystal growth (propagation of the crystal) on the strength of the confining force. However, the system did not show any significant changes in variation of other parameters including angular acceleration and viscosity.

Confining potential of the rotating fluid

When the cylinder rotates with high speed, we can assume the system to be in solid-body rotation and ignore gravity. In this regime the beads do not move relative to the liquid, and our system minimizes energy:

$$V(\rho_l - \rho_p)\,\omega^2 \sum_i r_i^2$$

Here V is the volume of the bead, ρ_l and ρ_p the densities of the liquid and the bead respectively, ω the angular velocity, and r_i the distance from the center of *i*-th bead to the cylinder axis. This is equivalent to minimizing $\sum_i r_i^2$ at a given concentration of the beads.

Surprisingly, the tubular packings observed at low concentrations are the same as the packings in a very different problem known in the literature: the problem of maximum volume-fraction configurations of hard spheres confined in a cylindrical channel (*32*,*33*). There are two key differences between this problem and our system. Firstly, the only parameter in the hard confinement problem is a size ratio of the confining cylinder and the sphere. Secondly, the harmonic potential $\sum_i r_i^2$ of our system is much softer than hard-contact potential of the confining cylinder. While theoretical and numerical models (*34–36*) predicted a numerous tubular packing at various size ratios of the cylinder and the sphere, very few studies have obtained those structures in experiments (*37–39*). In studies of the hard confinement problem, many numerical studies predicted the existence of various ordered structures at arbitrarily high concentrations, but in our system regular structures emerged only below a certain concentration. This discrepancy arises from the fact that the ordered structures that is expected to exist at high concentrations inevitably require an empty channel in the core of the structure, but the harmonic potential of our system does not favor the hollow core structure. This perspective is clearly presented in potential energy calculation in which the energy quickly increases from the point where hollow core structure starts to appear (cf. Figure 3c in chapter 2).

Repeated acceleration and deceleration for obtaining highly ordered structure

In this work, we have presented many examples of tubular structures with high and long-range ordering. It should be noted that most of the structures observed in single- and binary-component systems were not simply created by gradually increasing rotation rate from rest. We increased and decreased the rotation rate back and forth until a well-ordered structure was achieved. The improved ordering by the repetitive change of rotation rate can be attributed to the two facts: i) ordered structure is more stable than glassy packing; ii) an instantaneous change of rotation rate can induce transient flows along the tube's axis (cf. Figure 4 in chapter 2). When ordered and disordered packings coexist and are perturbed by the transient flows, it is more probable that the glassy packing is preferentially destroyed, and the composing particles reassemble into the coexisting ordered structure, resulting in a structure of long-range ordering. This way, some of the crystals easily formed within a relatively short time (less than 1 minute) and with a long-range ordering, while others required elaborate handling for its formation and/or exhibited a short-range ordering. Single component structures formed at high concentrations of particles and binary structures belong to the latter category.

Benefit from rotational motion

Intriguing feature of our system being in rotating frame of reference is marked when it is composed of two different types of spheres; diverse structures including 2-, 4-, 5-, and 6-fold rotational symmetries were created. What makes this diversity possible can be summarized into two factors. First, identical components occupy "identical" space; for example, all of the small spheres are in the core, whereas all of the large spheres in the shell. This can be achieved (and controlled) by the sequential approach of the spheres toward the cylinder axis, which are dependent on the density differences between the spheres and the liquid. Second, the rotational frame of reference provides the spheres with pathways long enough that the two components can be "separated" (or "isolated") during the crystallization process. To this end, the rotation rate should be increased gradually and slowly. On the other hand, another point to be addressed regarding the binary crystal is the range of the size ratios of the two components. The crystals reported in this study were formed by spheres of size ratios between 0.5 and 1. When the size ratio is less than ~0.4, the small spheres simply entered the interstitial sites of the structures formed by the large spheres.

1.3 3D fluidic trap and Hopf bifurcation.

House-made experimental system.

Our house-made system comprised components shown in **Figure 4** below. The headstock was purchased from Sherline Products Inc. (model 4100A) and motor from Oriental Motor co., Ltd (model BLE2D). The motor can be operated up to 4000 r.p.m. and precisely controlled by computer. Two magnets are placed on motorized stages (Thorlabs Inc., model MTS50-Z8) of which each is set to be separately controllable in order to generate asymmetric vortex-vortex trap. One side of the tube is mounted on the chuck of the headstock while the other side is held by a ball bearing which is inserted in a frame designed to move on the rail.

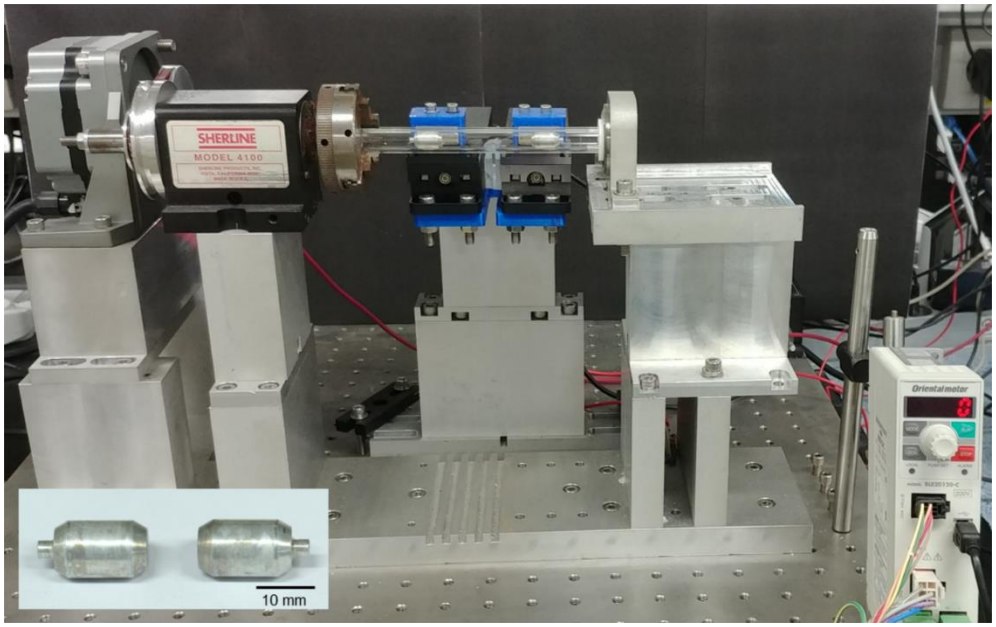

Figure 4. Photo of experimental set-up. Inset shows aluminum disks (radius 9.9 mm, thickness 16 mm) used in this study. The specific shape reflected technical considerations; the chamfers (1.5 mm × 2 mm) were designed for ease of insertion of the disks inside the tube and small tips (3 mm × 3 mm) aided manipulation of the disks by tweezers.

The aluminum disks which generate vortex flows were not fixed in lateral direction – they are free to move along the tube's axis. Under the given values of rotation rate and magnetic strength, the disks can find equilibrium lateral positions determined by vortex-vortex interaction and the flows bounced back from the both end walls (also see text in *Particle trapping by vortex-vortex interaction*). This lateral movement of the disks seems to in part lend non-linear behavior to the system which occasionally makes the dynamics of the system complex and unpredictable. Thus, by fixing the lateral position of the disks, one can extract essential features of the system in a more simple and efficient way.

Comments on the system's variables

In the main text of this work (Chapter 3), we used the rotation rate of the tube and the distance (d) between the magnet and the tube as two main parameters to vary the dynamics of the fluidic trap. However, more intrinsic parameter determining the system's behavior is the relative rotation rates of the disk and the tube (or the rotation rate of the disk), not d, once the geometry and surface property of the disk are determined. Thus, more complete and thorough picture of the system can be obtained by recording the relative rotation rates at every solution used (i.e., at various values of viscosities) and studying the relations of the system's behavior and this parameter. Using intrinsic parameters will increase our understanding on the system and might decrease the discrepancy between the experiment

and the simulation.

Particle trapping by vortex-vortex interaction

The vortices arising from the disks collide in the middle and spread radially-outward (spiral when viewed from the cross-section of the tube) pushing the particles away from the axis. On the other hand, the centripetal force, which is directed toward the axis of tube's rotation, attempts to keep the particles on the axis. A balance between the centripetal force and the drag force applied by the swirling flows determines the dynamics of the particles and the type of the packing (see **Figure 5**). If the centripetal force is much stronger than the drag force, the particles stay on the axis forming a single line or disordered packing. In contrast, if the drag force is dominant, the particles move following the complicated flow field developed between the disks – there is no stable region for the particles to stay. When the two forces are comparable, the particles can form ordered packing on the axis or draw ring-like trajectory in the colliding plane depending on the radial position at which the two forces cancel out. However, the dependence of the confining forces on the parameters is not simple. As seen in the phase diagram (Figure 2 in Chapter 3), the observation that the ordered packings are forbidden at the intermediate values of ω at d = 10 mm and 11 mm indicates non-linear nature of the relation. The non-linearity arises in part from the fact that the disks are free to move along the axis. Since on both sides of the disks are there flows bouncing back from the tube's cap and the colliding plane respectively, a balance of the forces applied by these flows determines the axial position of the disk. One last thing to consider in the particle trapping is the effect of the hydrodynamic forces by the assembly on the flows. The hydrodynamic force of the particles can be neglected for a small number of particles, but it is not when the particle's number density is high, or the size of the cluster is comparable to, for example, that of the disk. This effect can be seen from the fact that the phase behavior slightly varies with the number of particles since the presence of particle alters the local flow field of the fluid.

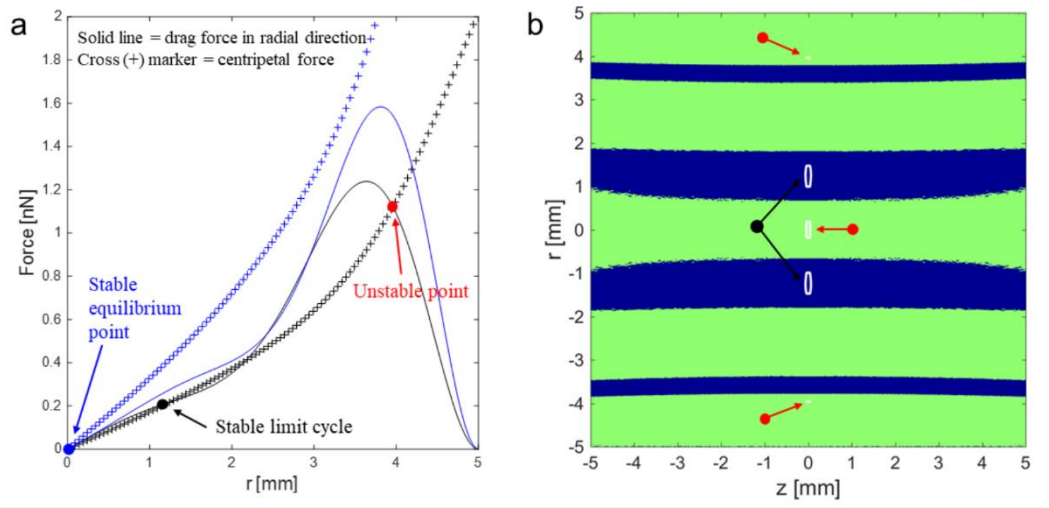

Figure 5. A balance between the centripetal and drag forces. a) Confining force curves for a stable equilibrium point (blue curve, ω = 1500 rpm) and a limit cycle (black curve, ω = 1000 rpm). Although there is another point where the two forces are canceled out, it is unstable due to the divergence of the force field. b) Partial derivatives of force field (color map) and near-zero-force lines (white) for the black curve in (a). Black and red dots indicate stable and unstable equilibrium point, respectively. Here, the simulation result is for 100 μm particle system at d = 7 mm.

The effect of the viscosity of the fluid and complexity of the vortex-vortex interaction

In our theoretical study (see Appendix in Chapter 3), it is possible to use a fluid of low viscosity if other conditions, such as rotational rate, are appropriately chosen. In reality, however, we could not obtain a reliable particle trapping in low viscosity liquids. Although we do not clearly understand the reason, we surmise that the vortex-vortex interaction might be unpredictably quite intricate and never cannot be depicted in laminar flow regimes, even for flows at low Reynolds number. This complexity of the interactions increases with no doubt for flows at higher Reynolds number (or in solutions of lower viscosity) and is represented in **Figure 6**. At relatively low rotation rate (ω = 2600 rpm), the microscopic particles are captured in a single layer of the flow, while there happen to exist other layers with increasing the rotation rate. Here, the solution is water, and the similar layered structure of the flow is also observed for other liquids of low viscosity ($\lesssim$ 2 mPa s). Consequently, our simulation study, which assumes the flows induced by the vortex-vortex interaction to be laminar flow, is considerably restricted and only applicable to approximate the behavior of the fluidic trap for small, trapping region. In order to get a full, precise portrait of the particle trapping, the flows should be at least estimated through 3D model allowing turbulent flow regimes. As a rule of thumb, the particle trapping could be obtained in a fluid of viscosity higher than ~2 mPa s.

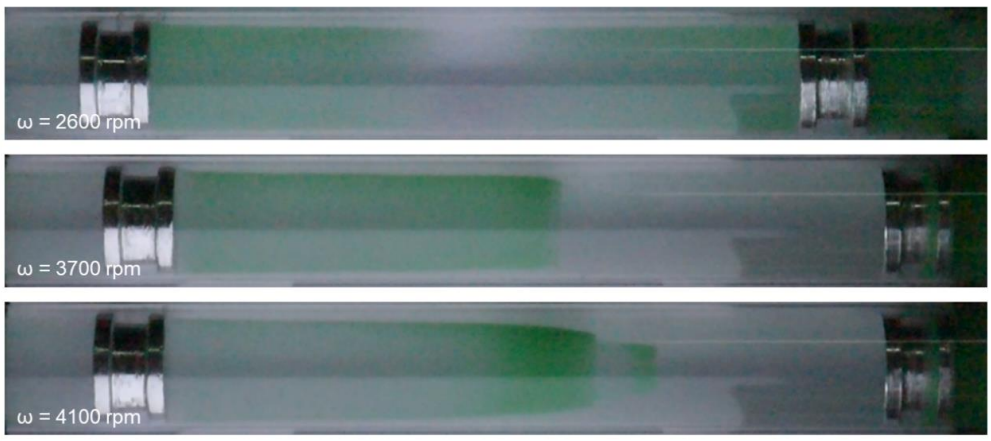

Figure 6. Complicated vortex-vortex interaction. Layered flow structure is induced by the vortex-vortex interaction and shown by tracer particles (50 μm). The complexity increases with the rotation

rate which is noted in each figure. Here, the fluid is water and *d* is 2 mm.

Key factors for structure determination and applicability

The variety of the dynamic assemblies demonstrated in this work is the output of questions that how widely and usefully the 3D fluidic trap can be utilized and how it is different from other trapping methods. If technical difficulty is excluded – which is not trivial but still achievable – particles up to sizes of a few micrometers can be, in principle, trapped (cf. Appendix in Chapter 3), indicating that a study on a microscale is feasible. We also want to emphasize that there are key factors in component-wise that regulates the type of assembly and its formation process: density difference between the particle and the fluid, size (or effective cross section), and moment of inertia. By combining these factors, we examined the applicability and utility of our trapping method. First, by mixing particles differing in densities, we demonstrated the selectivity in polymorphic structure: with 13 spheres which can theoretically assemble into many configurations (*40*), it was shown that particles of two different densities at various number ratios preferentially form one type over the possible other types of structures. This is one example of enhancement of the controllability over packings in our fluidic trap. Size variation in addition to the density variation could explore more diverse types of packings (cf. 'ring of Saturn' and 'cage' structures in Figure 4 in Chapter 3). Lastly, interesting demonstration of 'Rotaxane' structure was possible from the fact that the component rotates with an orientation that minimizes its moment of inertia with respect to the tube's axis. If the parameters are properly chosen – for example, ω = 800 rpm and d = 8 mm – such that the vortices can induce an array of rings with an altered orientation, the rod can enter through the array forming the targeted structure.

Our attempts to explore diverse packings continued to use polyhedron for building blocks – tetrahedron, square pyramid and cube (see **Figure 7**). Here, the motivation was to study shape-determining packings and dynamic process for polyhedral helixes. Although we could detect some possible assemblies and their formation processes, the nature of the complexity of polyhedral packing and technical issue (see caption in Figure 7) prevented us from a deep study. Last thing we want to note is the observation of the singularity of a droplet. While a single droplet shows gradual changes as the lateral confinement increases, it is elongated and transformed into several threads, and finally broken into many small droplets. The small droplets again formed a cluster in the trapping region, and this behavior repeatedly continued.

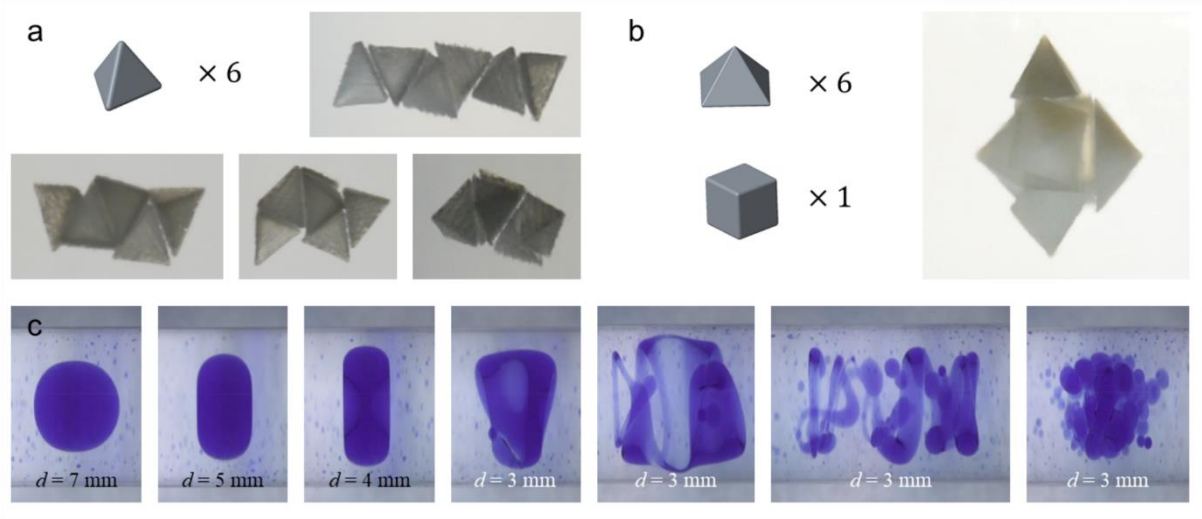

Figure 7. Polyhedral assemblies and singularity at critical point. a) Tetrahelix and other packings formed by 6 tetrahedrons – the edge length is 1.5 mm. b) An ordered cluster can be formed by surrounding one cube with 6 square pyramids – the edge length of the polyhedrons is 2 mm. It was more probable that the components were randomly arranged, and the formation of ordered packing was infrequently detected. Here, the polyhedrons were fabricated using 3D printer. Due to limited resolution of the 3D printer, the polyhedrons had rough surfaces and thus large frictions between them. The solution was a mixture of fluorinated liquid (3M Novec 7200 Engineered Fluid) and silicone oil (PDMS, viscosity 10 cSt, Sigma Aldrich) in a 7/3 v/v ratio. c) A droplet showed the singularity at a critical point – d = 3 mm and ω = 1000 rpm. Here, oleic acid forms the droplet in fluorinated liquid (3M Novec 7200 Engineered Fluid).

Different bifurcation behavior depending on the rotational rate

One of the fascinating features of our system is the transition between a stable point ("stable equilibrium") and an orbiting motion ("limit cycle") which is also known as Hopf bifurcation in the theory of dynamical system. In particular, we proved the existence of two limit cycles using 100 μm particle at ω = 1800 rpm and presented the bifurcation diagram with d as a control parameter. (see Chapter 3 for details). It is worth noting that the bifurcation can also be very different depending on the rotational rate. In **Figure 8**, we show bifurcation diagrams for the system consisting of 100 μm particle at various rotational rates. As seen from the figures, the system can exhibit very different transition behavior among the 4 states: a stable point, one limit cycle, two limit cycles and one limit cycle/a stable point.

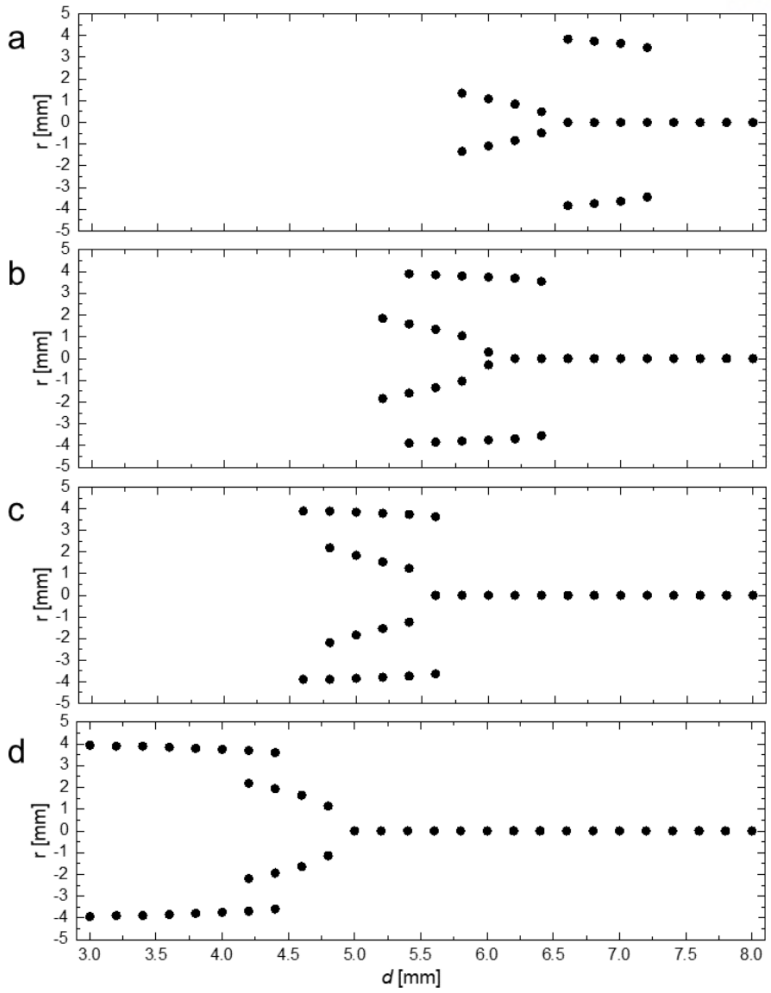

Figure 8. Bifurcation diagrams at various rotational rates. The system consisting of 100 μm particle can show different bifurcations at the rotational rates of (a) 1000 rpm, (b) 1400 rpm, (c) 1600 rpm and (d) 2000 rpm.

1.4 Related work

During my doctoral course, I also co-authored one paper which is another system that we achieved in the rotational frame of reference. The reference is:

Gizynski, K.; Lee, T.; Grzybowski, B.A. Dynamic Self-Assembly of Magnetic/Polymer Composites in Rotating Frames of Reference. *Adv. Mater.* **2017**, *29*, 1700614.

References

[1] Fialkowski, M.; Bishop, K. J. M.; Klajn, R.; Smoukov, S. K.; Campbell, C. J.; Grzybowski, B. A. Principles and Implementations of Dissipative (Dynamic) Self-Assembly. *J. Phys. Chem. B* **2006**, 110, 2482–2496.

[2] Warren, J. A.; Boettinger, W. J.; Prediction of Dendritic Growth and Microsegregation Patterns in a Binary Alloy Using the Phase-Field Method. *Acta Metall. Mater.* **1995**, 43, 689–703.

[3] Christiansen, B.; Alstrom, P.; Levinsen, M. T.; Ordered Capillary-Wave States: Quasicrystals, Hexagons, and Radial Waves. *Phys. Rev. Lett.* **1992**, 68, 2157–2160.

[4] Grzybowski, B. A.; Stone, H. A.; Whitesides, G. M.; Dynamic Self-Assembly of Magnetized, Millimetre-Sized Objects Rotating at a Liquid–Air Interface. *Nature* **2000**, 405, 1033–1036.

[5] Snezhko, A.; Aranson, I. S.; Magnetic Manipulation of Self-Assembled Colloidal Asters. *Nat. Mater.* **2011**, 10, 698–703.

[6] Yan, J.; Bloom, M.; Bae, S.C.; Luijten, E.; Granick, S. Linking Synchronization to Self-Assembly Using Magnetic Janus Colloids. *Nature* **2012**, *491*, 578-581.

[7] Li, T.; Kheifets, S.; Medellin, D.; Raizen, M. G.; Measurement of the Instantaneous Velocity of a Brownian Particle. *Science* **2010**, 328, 1673-1675.

[8] Anderson, M. H.; Ensher, J. R.; Matthews, M. R.; Wieman, C. E.; Cornell, E. A. Observation of Bose-Einstein Condensation in a Dilute Atomic Vapor. *Science* **1995**, *269*, 198-201.

[9] Wang, M. D.; Yin, H.; Landick, R.; Gelles, J.; Block, S. M. Stretching DNA with Optical Tweezers. *Biophys. J.* **1997**, *72*, 1335-1346.

[10] de Vries, A. H. B.; Krenn, B. E.; van Driel, R.; Subramaniam, V.; Kanger, J. S. Direct Observation of Nanomechanical Properties of Chromatin in Living Cells. *Nano Lett.* **2007**, *7*, 1424-1427.

[11] Barredo, D.; Lienhard, V.; de Léséleuc, S.; Lahaye, T.; Browaeys, A. Synthetic Three-Dimensional Atomic Structures Assembled Atom by Atom. *Nature* **2018**, *561*, 79-82.

[12] Ashkin, A. Acceleration and Trapping of Particles by Radiation Pressure. *Phys. Rev. Lett.* **1970**, *24*, 156-159.

[13] Ashkin, A.; Dziedzic, J. M. Optical Trapping and Manipulation of Viruses and Bacteria. *Science* **1987**, *235*, 1517-1520.

[14] Jonáš, A.; Zemánek, P.; Light at Work: The Use of Optical Forces for Particle Manipulation, Sorting, and Analysis. *Electrophoresis* **2008**, 29, 4813–4851.

[15] Strick, T. R.; Allemand, J.-F.; Bensimon, D.; Bensimon, A.; Croquette, V. The Elasticity of a Single Supercoiled DNA Molecule. *Science* **1996**, *271*, 1835-1837.

[16] Zhang, C.; Khoshmanesh, K.; Mitchell, A.; Kalantar-zadeh, K. Dielectrophoresis for

Manipulation of Micro/Nano Particles in Microfluidic Systems. *Anal. Bioanal. Chem.* **2010**, *396*, 401-420.

[17] Marzo, A.; Seah, S. A.; Drinkwater, B. W.; Sahoo, D. R.; Long, B.; Subramanian, S. Holographic Acoustic Elements for Manipulation of Levitated Objects. *Nat. Commun.* **2015**, *6*, 8661.

[18] Sundararajan, N.; Pio, M. S.; Lee, L. P.; Berlin, A. A. Three-Dimensional Hydrodynamic Focusing in Polydimethylsiloxane (PDMS) Microchannels. *J. Micro-mech. Syst.* **2004**, *13*, 559-567.

[19] Karimi, A.; Yazdi, S.; Ardekani, A. M. Hydrodynamic Mechanisms of Cell and Particle Trapping in Microfluidics. *Biomicrofluidics* **2013**, *7*, 021501.

[20] Chiou, P. Y.; Ohta, A. T.; Wu, M. C.; Massively Parallel Manipulation of Single Cells and Microparticles Using Optical Images. *Nature* **2005**, 436, 370-372.

[21] Escobedo, C.; Brolo, A. G.; Gordon, R.; Sinton, D.; Optofluidic Concentration: Plasmonic Nanostructure as Concentrator and Sensor. *Nano Lett.* **2012**, 12, 1592-1596.

[22] Gursul, I. Review of Unsteady Vortex Flows over Slender Delta Wings. *J. Aircr.* **2005**, 436, 299-319.

[23] Whale, J.; Anderson, C. G.; Bareiss, R.; Wagner, S. An Experimental and Numerical Study of the Vortex Structure in the Wake of a Wind Turbine. *J. Wind Eng. Ind. Aerody.* **2000**, 84, 1-21.

[24] Kawai, H. Local Peak Pressure and Conical Vortex on Building. *J. Wind Eng. Ind. Aerody.* **2002**, 90, 251-263.

[25] Hattori, Y.; Fukumoto, Y. Modal Stability Analysis of a Helical Vortex Tube with Axial Flow. *J. Fluid Mech.* **2014**, 738, 222-249.

[26] Scheeler, M. W.; van Rees, W. M.; Kedia, H.; Kleckner, D.; Irvine, W. T. M. Complete Measurement of Helicity and its Dynamics in Vortex Tubes. *Science* **2017**, 357, 487-491.

[27] Boersma, J.; Wood, D. H. On the Self-Induced Motion of a Helical Vortex. *J. Fluid Mech.* **1999**, 384, 263-279.

[28] Hardin, J. C. The Velocity Field Induced by a Helical Vortex Filament. *Phys. Fluids* **1982**, 25, 1949-1952.

[29] Alkhaddar, R. M; Higgins, P. R.; Phipps, D. A.; Andoh, R. Y. G. Residence Time Distribution of a Model Hydrodynamic Vortex Separator. *Urban Water* **2001**, 3, 17-24.

[30] Zhang, Q.; Wang, L.-B.; Zhang, Y.-H. The Mechanism of Heat Transfer Enhancement Using Longitudinal Vortex Generators in a Laminar Channel Flow with Uniform Wall Temperature. *Int. J. Therm. Sci.* **2017**, 117, 26-43.

[31] Agarwal, K. K.; Krishna, S.; Ravikrishna, R. V. Mixing Enhancement in a Compact Trapped Vortex Combustor. *Combust. Sci. Technol.* **2013**, 185, 363-378.

[32] Pickett, G.T.; Gross, M.; Okuyama, H. Spontaneous Chirality in Simple Systems. *Phys. Rev. Lett.* **2000**, *85*, 3652-3655.

[33] Mughal, A.; Chan, H.K.; Weaire, D. Phyllotactic Description of Hard Sphere Packing in Cylindrical Channels. *Phys. Rev. Lett.* **2011**, *106*, 115704.

[34] Erickson, R.O. Tubular Packing of Spheres in Biological Fine Structure. *Science* **1973**, 181, 705-716.

[35] Mughal, A.; Chan, H.K.; Weaire, D.; Hutzler, S. Dense Packings of Spheres in Cylinders: Simulations. *Phys. Rev. E* **2012**, *85*, 051305.

[36] Fu, L.; Steinhardt, W.; Zhao, H.; Socolar, J.E.S.; Charbonneau, P. Hard Sphere Packing within Cylinders. *Soft Matter* **2016**, *12*, 2505-2514.

[37] Mickelson, W.; Aloni, S.; Han, W.Q.; Cumings, J.; Zettl, A. Packing C_{60} in Boron Nitride Nanotubes. *Science* **2003**, *300*, 467-469.

[38] Tymczenko, M.; Marsal, L.F.; Trifonov, T.; Rodriguez, I.; Ramiro-Manzano, F.; Pallares, J.; Rodriguez, A.; Alcubilla, R.; Meseguer, F. Colloidal Crystal Wires. *Adv. Mater.* **2008**, *20*, 2315-2318.

[39] Li, F.; Badel, X.; Linnros, J.; Wiley, J.B. Fabrication of Colloidal Crystals with Tubular-like Packings. *J. Am. Chem. Soc.* **2005**, *127*, 3268-3269.

[40] Conway, J. H.; Sloane, N. J. A. *Sphere Packings, Lattices, and Groups*, Springer, New York, **1999**.

Chapter 2. Non-Equilibrium Self-Assembly of Monocomponent and Multicomponent Tubular Structures in Rotating Fluids

2.1 Abstract

When suspended in a denser rotating fluid, lighter particles experience a cylindrically symmetric confining potential that drives their crystallization into either monocomponent or unprecedented binary tubular packing. These assemblies form around the fluid's axis of rotation, can be dynamically interconverted (upon accelerating or decelerating the fluid), can exhibit preferred chirality, and can be made permanent by solidifying the fluid. The assembly can be extended to fluids forming multiple concentric interfaces or to systems of bubbles forming both ordered and "gradient" structures within curable polymers.

2.2 Introduction

Packing of particles over (or inside) cylindrical domains has been studied for well over a century, initially in the context of leaves arranging around a plant's stem, scales on a pine cone, or spines on a cactus (the so-called "phyllotaxis" (*1,2*)). Subsequently, such forms of "tubular" packing have also been observed in bacteriophage tails, bacterial flagella, and microtubules (*3*) as well as various material systems (e.g., foams (*4,5*), colloids (*6,7*), and nanoparticles (*8*) in templating channels, fullerenes in nanotubes (*9,10*), fibrous assemblies of Janus particles (*11*), chiral nanoparticles (*12*), or DNA (*13*)). While the packing of equally sized particles has been studied theoretically and understood in detail (*3,14–17*), it has proven difficult to *a priori* predict/control assembly of specific structures in experiment. In addition, there have been no works that would consider tubular packing in mixtures of particles of different sizes. Here, we describe non-equilibrium self-assembly (*18,19*) of ordered tubular structures which relies not only on molecular- or colloidal-scale particle–particle interactions (*6–13*) but also on fluidic confinement imposed by a rotating fluid (*20*) denser than the assembling particles. By adjusting the sizes and numbers of these particles, it is then possible to form monocomponent as well as unprecedented binary tubular assemblies ranging from those having many (D_{4d}, D_{6h}, etc.) to very few (C_s) symmetry elements. The system we describe combines four other remarkable characteristics: i) the strength of the confinement can be regulated by the fluid's rate of rotation; ii) different tubular structures can be interconverted by accelerating or decelerating the fluid; iii) for the helical assemblies, it is possible to control their chirality by adjusting the orientation of the fluid's axis of rotation with respect

to gravity; and iv) the transient assemblies can be made permanent by solidifying the rotating liquid. The experimental results are supported by molecular dynamics simulations and, together, constitute a generalizable toolkit for the assembly of fibrous structures of unusual symmetries and with interesting

extensions to the problems of packing of nonspherical particles (*21,22*) or deformable entities (e.g., bubbles, cells) in adjustable, fluid-imposed confinements.

Figure 1a illustrates the experimental system in which polymeric beads (density ρ_p = 0.9–1.13 g cm^{-3} depending on the material used) are placed in a cylindrical tube (I.D. 10 mm; O.D. 15 mm; length, L = 75 mm) filled with an aqueous solution of agarose (≈0.25 wt%, Calbiochem Omnipur Agarose) and with cesium bromide added to adjust the density of the liquid to above that of the particular beads used (ρ_l = 1–1.2 g cm^{-3}). The tube is sealed (so that no air bubbles remain inside) and mounted onto a commercial lathe (Sherline Products 4100A-DRO) for which the angular velocities can be adjusted up to ω = 10 000 rpm. To prevent agarose gelation, the system is kept at 60 °C. When the tube is stationary or rotates along its long axis only slowly (cf. below), the dynamics of the beads is dominated by the buoyant force directed upward, $\boldsymbol{F}_B = (\rho_p - \rho_l)\mathrm{V}\boldsymbol{g}$, where V is bead's volume and $\boldsymbol{g}$ is gravity. When ω increases, however, the beads start to experience a centripetal force directed toward the axis of tube's rotation, $\boldsymbol{F}_C(\boldsymbol{r}) = -(\rho_l - \rho_p)\mathrm{V}\boldsymbol{r}\omega^2$, where vector $\boldsymbol{r}$ specifies bead's radial position. In other words, the rotation of the tube imposes a confining harmonic potential on the beads, $\mathrm{E}(\boldsymbol{r}) = 1/2(\rho_l - \rho_p)\ \mathrm{V}\boldsymbol{r}^2\omega^2$. As the rotation rate is increased to a few thousand rpm, centripetal acceleration increases to the order of 10 g, and the centripetal force localizes the beads toward the axis of tube's rotation. When the number of beads is low, they can all fit into a single line on the axis of rotation. When however, there are significantly more beads, they form ordered cylindrical structures such as those shown in Figure 1b–d. Importantly, these tubular assemblies can be made permanent–without any change in ordering—by gelating the agarose solution by letting the rotating tube cool down to room temperature. Examples of such solidified structures are shown in Figure 1c,d.

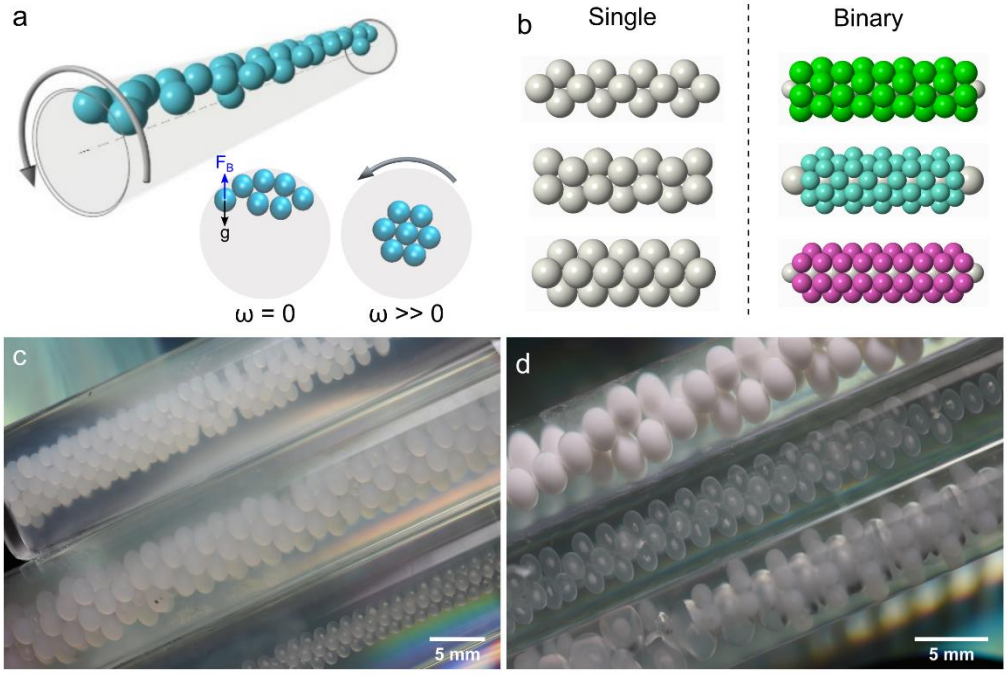

Figure 1. Experimental arrangement and examples of mono- and multicomponent tubular assemblies. a) Scheme of the experimental system. Directions of gravity (***g***) and of the buoyant force ($\boldsymbol{F}_B$) are indicated by arrows. b–d) Cartoons (b) and experimental images (c,d) of some of the structures assembled at/around the cylinder's axis of rotation. The structures shown in the photographs were made permanent by gelating the agarose solution. In (c), the top structure is a binary assembly of 1.588 mm polyamide shell particles and 2.381 mm polypropylene core particles; the middle structure comprises 2.381 mm polyamide (shell) and 1.588 mm polypropylene (core) beads; the bottom structure is a monocomponent assembly of 1.588 mm polypropylene beads. In (d), the top and middle structures are monocomponent (made of, respectively, 2.45 mm polypropylene and 1.588 mm polypropylene beads). The bottom structure is a binary assembly 1.588 mm polyamide (shell) and 3.175 mm polypropylene (core) particles. Scale bars = 5 mm.

2.3 Tubular structure formation of like-sized particles: experiment and simulation

We first consider structures formed by like-sized particles – in most experiments, d = 1.588 mm polypropylene spheres (ρ = 0.9 g cm^{-3}), but also 53 and 500 μm polyethylene spheres (ρ = 0.98 g cm^{-3}). **Figure 2**a–e show structures obtained at ω = 2000–3000 rpm. when the number of the millimeter-sized particles (nondimensionalized by the number of spheres forming a tightly packed single line along the tube, $n_0 = L/d$; also see caption in Figure 2) was increased from 1.2 to 4.0. These structures comprise both helical assemblies of different pitch as well as those of D_{2d} and D_{3d} symmetries, all previously predicted (*3*,*15*,*16*,*23*,*24*) (but only few observed experimentally (*6*–*9*,*11*)) for the maximum-volume-fraction configurations of hard spheres confined in a cylindrical channel.

Amorphous phase begins to occur at $n/n_0 \approx 3.0$, becomes significant at $n/n_0 \approx 3.8$ (accompanying structures of D_{2d} symmetry), and dominates above $n/n_0 \approx 4.5$. The full ω versus n/n_0 phase diagram is shown in Figure 2f and features several regions where different types of packing can coexist within the tubular aggregates – in such cases, larger markers denote the dominant "polymorphs." We note that structures observed for larger particles also assemble from smaller beads (500 and 53 μm, Figure 2g,h), although achieving good quality packing requires much more experimental care, especially eliminating even minor off-axis precession of the tube in the lathe and careful reduction of any vibrations.

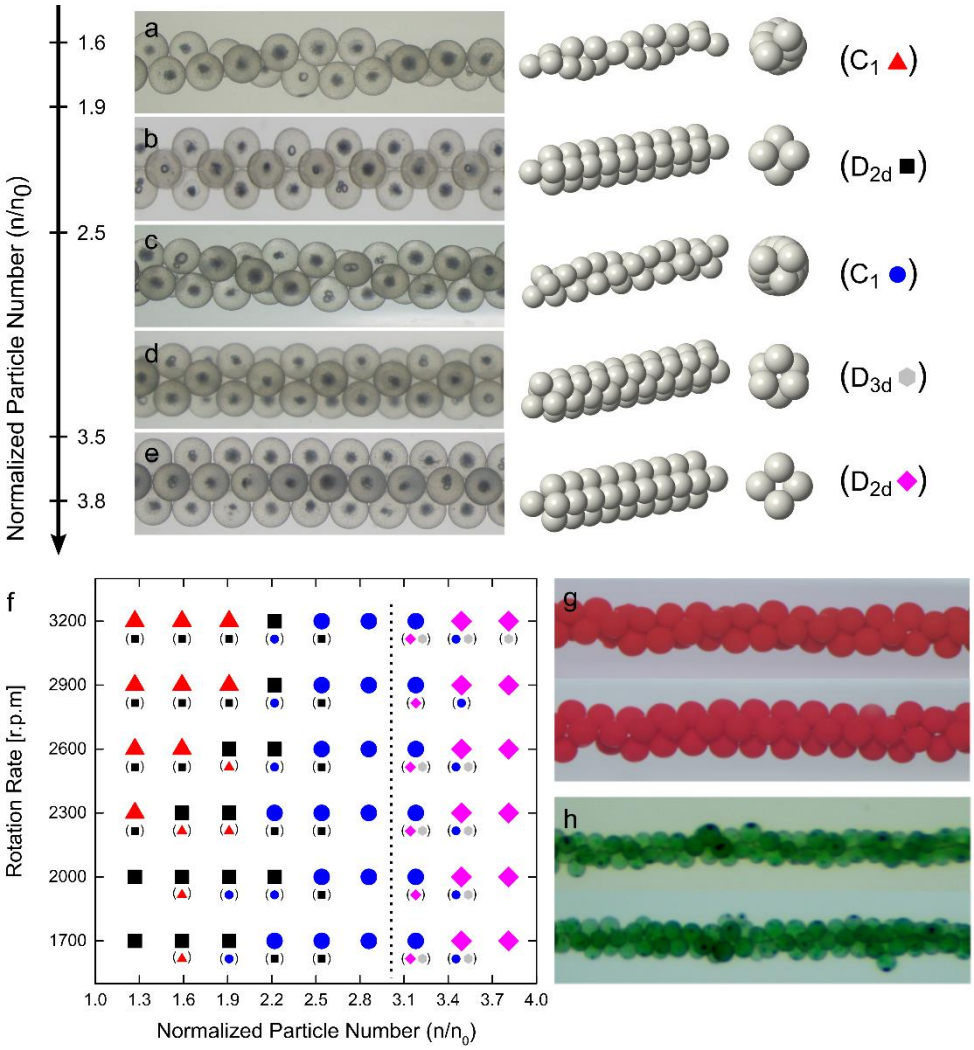

Figure 2. Monocomponent tubular assemblies. a–e) Representative structures formed by 1.588 mm polypropylene beads immersed in a mixture of water and agarose at ω = 2000–3000 rpm. Experimental images are shown in the left column; 3D and cross-sectional cartoons are shown on the right. The vertical axis gives the number n of the spheres relative to the number n_0 of spheres in a

tightly packed single line of length equal to that of the tube. f) A phase diagram indicating dominant structures at different values of ω and n/n_0. Structures are denoted by different markers corresponding to those in panels (a–e). If the assemblies are polymorphic – that is, feature regions of different packing – larger markers correspond to the dominant structure. At concentrations higher than $n/n_0 \approx 3.0$ (dotted line), the assemblies also contain noticeable fractions of amorphous phase. Images of structures formed by smaller, g) 500 μm and h) 53 μm (h), particles at ω = 2000–3000 rpm.

To obtain further insights into the assembly process, we performed molecular dynamics simulations following the general methods (*25*,*26*) to describe motion of particles or bubbles in rotational flows. In brief, the time changes in the velocity $\mathbf{v_i}$ of sphere *i* are due to several forces, $\rho_p V \frac{d\mathbf{v_i}}{dt} = \mathbf{F}_A^i + \mathbf{F}_I^i + \mathbf{F}_D^i + \mathbf{F_B} + \mathbf{F}_L^i + \mathbf{F}_{ij}^n$. In this equation, $\mathbf{F}_A^i = \rho_l C_M V \left(\frac{D\mathbf{u_i}}{Dt} - \frac{d\mathbf{v_i}}{dt}\right)$ accounts for the motion of a sphere in an inviscid flow of velocity $\mathbf{u_i}$ and with an added-mass coefficient (*27*) C_M, $\mathbf{F}_I^i = \rho_l V \left(\frac{D\mathbf{u_i}}{Dt}\right)$ is the inertial force, $\mathbf{F}_D^i = \frac{1}{2} C_D A \rho_l |\mathbf{u_i} - \mathbf{v_i}|(\mathbf{u_i} - \mathbf{v_i})$ is a drag force (*25*) in a viscous fluid with C_D being the drag coefficient and *A* the cross-sectional area of the sphere, and $\mathbf{F_B} = (\rho_p - \rho_l)V\mathbf{g}$ is the buoyant force. In a rotational flow, the sphere also experiences a lift force (*28*) $\mathbf{F}_L^i = \rho_l C_L V(\boldsymbol{u_i} - \boldsymbol{v_i}) \times (\nabla \times \boldsymbol{u_i})$, where C_L is the lift coefficient. To capture interactions between polymeric, slightly deformable spheres *i* and *j* with the overlap $\alpha_{ij} = |\boldsymbol{r}_i - \boldsymbol{r}_j| - d$, we adopted the "partially latching spring" model (*29*) with a normal contact force: $\mathbf{F}_{ij}^n = K_1 \alpha_{ij} \boldsymbol{n}_{ij}$ ($\alpha_{ij}, \geq 0$, loading) or $\mathbf{F}_{ij}^n = K_2(\alpha_{ij} - \alpha_o)\boldsymbol{n}_{ij}$ ($\alpha_{ij} \leq 0$, unloading), where K_1 and K_2 are the stiffness coefficients for loading and unloading, respectively, α_o is the value of α_{ij} where the unloading curve goes to zero, and $\boldsymbol{n}_{ij} = (\boldsymbol{r}_i - \boldsymbol{r}_j)/|\boldsymbol{r}_i - \boldsymbol{r}_j|$ is the unit vector joining the centers of the two spheres. Hydrodynamic interactions between sparsely distributed particles were not necessary to simulate the tightly-packed assemblies forming for $n/n_0 > 1$.

The simulations reproduce all experimentally observed structures (e.g., **Figure 3**a) including dominant vs minority packing (see above and also phase diagram in Figure 3d) and appearance of an amorphous phase at high concentrations ($n/n_0 \gtrsim 3.7$). Figure 3b plots the fractions of ordered domains of a given packing (quantified by the total length of such ordered domains relative to the entire length of the assembly/tube, *L*) as a function of the normalized particle number n/n_0. As seen and in agreement with experiments, the fraction of ordered domains decreases with increasing n/n_0 and is the lowest for structures that have voids along the axis of rotation (D_{3d}, gray line and D_{2d}, pink line). Interestingly, in previous theoretical studies of hard spheres packing in rigid cylinders (*3*,*23*), all large structures (i.e., those formed in cylinders much wider than particle diameter) featured an empty channel along the cylinder's long axis. In our harmonic potential, however, such structures are

energetically very costly (cf. energies calculated in Figure 3c) which can explain why they are of less regular ordering and also why for even higher particle numbers, we observe mostly glassy states.

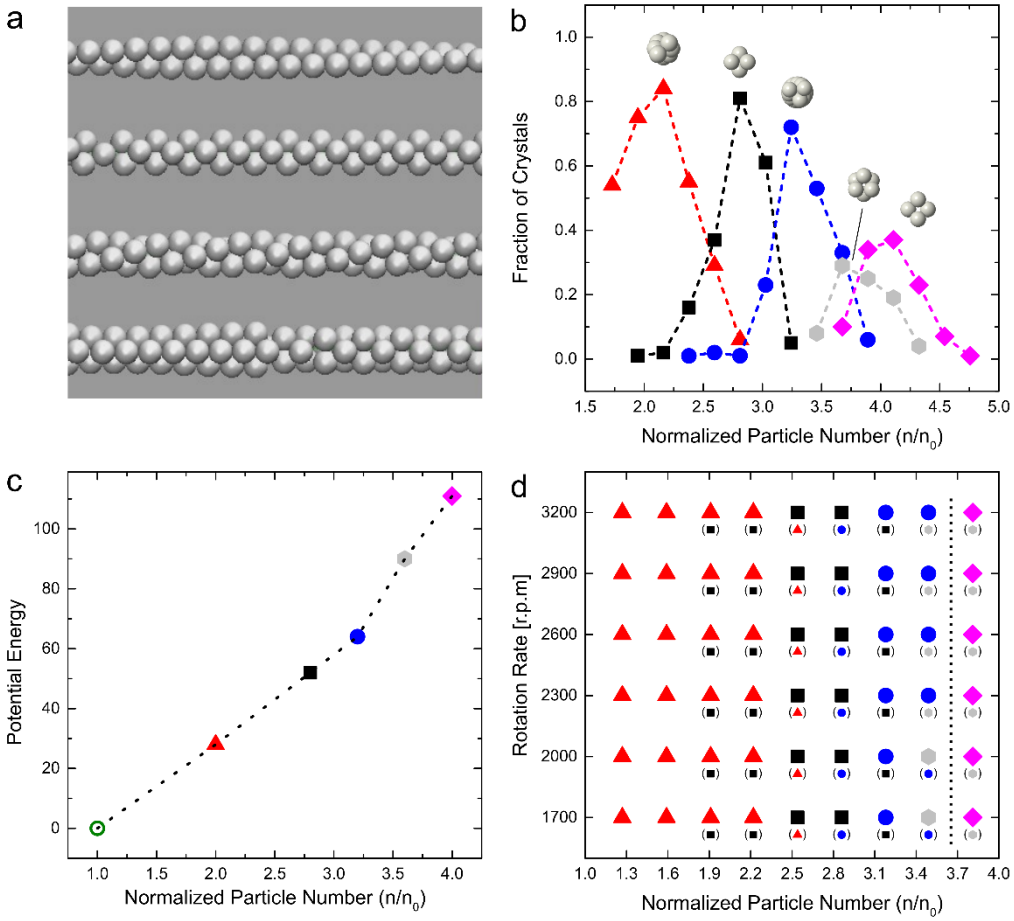

Figure 3. Simulations of monocomponent tubular structures. a) Examples of structures simulated by molecular dynamics. b) Fraction of ordered assemblies of a given packing plotted as a function of n/n_0 (i.e., particle number relative to the number of particles packed in a single straight line along tube's axis of rotation). Cross-sectional images of structures are given by the cartoons over each curve; compare with Figure 2a-2e. Each data point corresponds to an average from ten independent simulation runs (here, for ω = 3,500 rpm., L = 75 mm, ID_{tube} = 10 mm, d = 2 mm, ρ_l = 1.0 g cm^{-3}, ρ_p = 0.9 g cm^{-3}). c) Potential energy of tubular assemblies as a function of the normalized particle number, n/n_0. The energy is in the units of $\rho_l V\omega^2$ with the "zero" reference point corresponding to a line formed by n_0 particles. Calculations were performed for 2 mm particles and 75-mm-long tube. d) A simulated phase diagram (compare with Figure 2f) indicating dominant (large markers) and minority (smaller markers in parentheses) structures observed at different values of ω and n/n_0. Amorphous phase becomes appreciable at concentrations above n/n_0 ~ 3.7 (dotted line). Ten independent simulations were carried out for each condition (with L = 50 mm, ID_{tube} = 10 mm,

d = 1.588 mm, ρ_l = 1.0 g cm^{-3}, ρ_p = 0.9 g cm^{-3}). Rotation rate was increased from rest to a desired angular velocity with acceleration of 100 radians sec^{-2} (16 revolutions sec^{-2}).

2.4 Interconversion between structures and selective helicity

We make two additional comments about the monocomponent assemblies. First, at least some structures can be interconverted by changing the rotation rate (e.g., in **Figure 4**a, from D_{2d} into C_1 and from C_1 to D_{3d} by decreasing rotation rate). This phenomenon is due to the fact that upon changes in ω, the fluid near the tube's surface and side walls responds first, effectively giving rise to transient flows along the tube's axis (Figure 4b) (*30*). Depending on whether the fluid is accelerated or decelerated, these flows either stretch or compress the beads along the axis of rotation, resulting in the change in their packing. Interestingly, such transitions are fully reversible when the changes in the rotation rates are rapid (on the order of 100 rpm s^{-1}) – under these circumstances, strong transient flows are induced and the particles are disrupted enough to fully convert to another structure. In contrast, when the changes in ω are slow (up to ≈ 10 rpm s^{-1}), the transient flows at any instant of time are weak and the structure remains trapped/jammed. In other words, the system can exhibit bistability in the sense that two different types of assemblies can be prepared at the same value of ω depending on how this state was reached (again, via rapid or slow changes in rotational speed).

Second, Second, when the rotating tubes were horizontal, there was no preference for the chirality of the helical structures that form. Lack of chiral selection was also confirmed in molecular dynamics simulations which we repeated 100 times, each time starting from random positions of beads. The ratio of right- to left-handed helices was 52:48. However, such chiral selection is observed when the tube is inclined. Under such conditions, the beads first localize near the side wall pointing upward (inset images in Figure 4c) and then, when the tube starts rotating, experience friction with respect to this rotating wall and ultimately form helices of preferred handedness (main images in Figure 4c,). For a given direction of rotation, this chirality depends on which end of the tube is raised upward and the enantiomeric excess – determined based on 100 independent experiments for each configuration – can be as high as 80% (Figure 4d). The chiral selection is also reproduced in simulations.

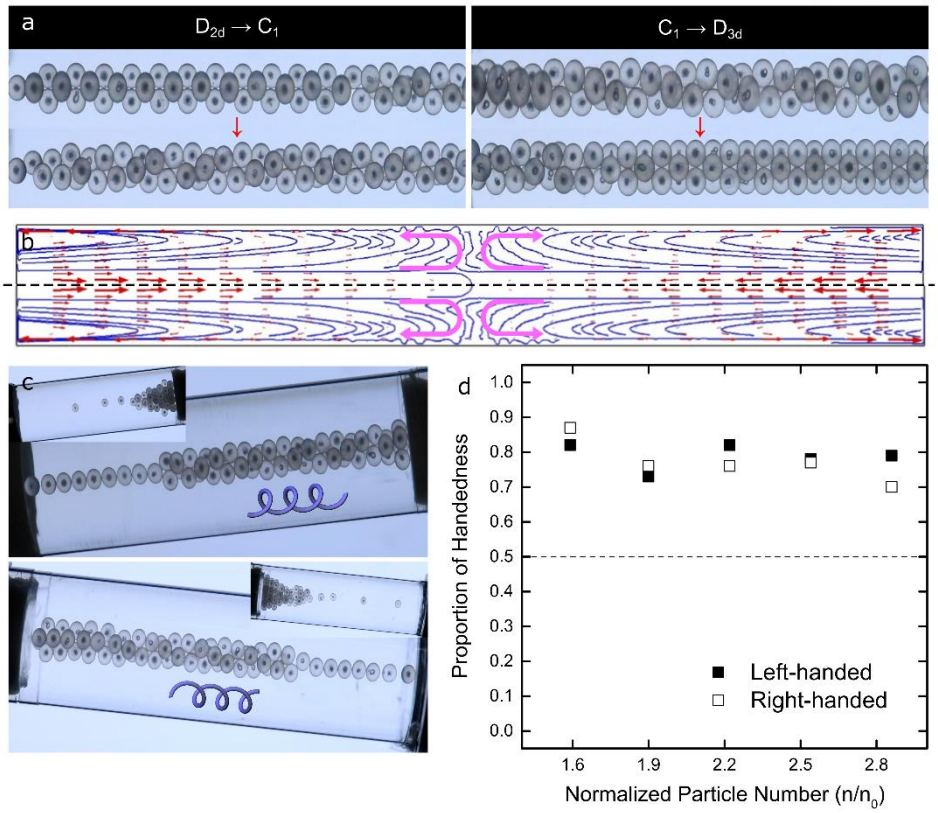

Figure 4. Phase transitions between different structures and chiral selection. a) Two experimental images for structural transition from D_{2d} to C_1 (at n/n_0 = 2.4), and from C_1 to D_{3d} (at n/n_0 = 3.2) structures. In both cases, rotation rate was abruptly decreased from ~4,000 to ~1,500 rpm. so that the beads experienced a "compressing" force along the tube's length. b) Transient flow of the fluid developed upon rapid deceleration of tube's rotation. The flow was calculated in Comsol 5.1 (*30*) by decreasing the rotation rate from 3,000 rpm (t = 0 sec) to 1,500 rpm (t = 1 sec; shown). Blue lines trace the streamlines and red arrows are velocity vectors. Curved, pink arrows are qualitative and illustrate the overall nature of the flow. c) Formation of left-handed (*upper*) and right-handed (*lower*) helices in inclined rotating tubes. Here, the tube's axis is oriented by 8 degrees with respect to gravity, and the rotation rate is increased from 0 to 2,500 rpm. d) Statistics of handedness of helices formed in each of the two orientations from (c). The proportions are estimated by analyzing 100 independent experiments for each condition.

2.5 Binary component tubular packing: experiment and simulation

Having characterized the monocomponent packing, we turned our attention to those comprising two different types of particles – such tubular structures have not been previously considered theoretically or observed experimentally. In these experiments, we used polypropylene (ρ = 0.9 g cm^{-3}) and polyamide (ρ = 1.13 g cm^{-3}) beads with diameters d = 1.588, 2, 2.381, or 3.175 mm and added cesium bromide to the agarose solution to increase the density to $\rho \approx$ 1.2 g cm^{-3}. Importantly, when in a

rotating fluid, the lighter beads localized to the axis of rotation preferentially. In most experiments, the number of lighter beads was relatively small such that they could all fit onto the axis of rotation. The denser beads then packed as a "shell" around this "core". Various two-component structures assembled in this manner are shown in **Figure 5**a–f. When the spheres at the core are larger than those in the shell, assemblies of six-fold rotational symmetries are observed at size ratios of $d_{shell}/d_{core} \approx 0.50$ (Figure 5a) and 0.67 (Figure 5b); in the former case, each core sphere has 18 neighbors, in the latter, it has 12 neighbors. When $d_{shell}/d_{core} > 1$, structures of four-fold and five-fold symmetries assemble at size ratios of 1.26 (Figure 5c) and 1.50 (Figure 5d). On the other hand, the spheres of equal sizes can form two polymorphs shown in Figure 5e,f, both of which have one core sphere and six shell spheres in a unit cell (the difference in packing is further illustrated in schematic figure insets). We note that in all of the above examples, achieving highly organized structures is crucially dependent on increasing ω slowly, at rate of ≈ 10 rad s^{-2}; if the rotational rate is increased abruptly, some of the denser spheres can block the approach of the lighter ones to the axis of rotation and the assemblies are disordered. Also, good quality structures are formed by spheres of size ratios (d_{small}/d_{large}) down to ≈ 0.5. When this size ratio is lower, the small spheres simply enter the interstitial sites between the larger spheres and become jammed therein. We note that simulations based on the same methodology as described before reproduce the formation of all of the experimentally observed structures (Figure 5g,l) although regular packing near the tube's side walls is harder to achieve.

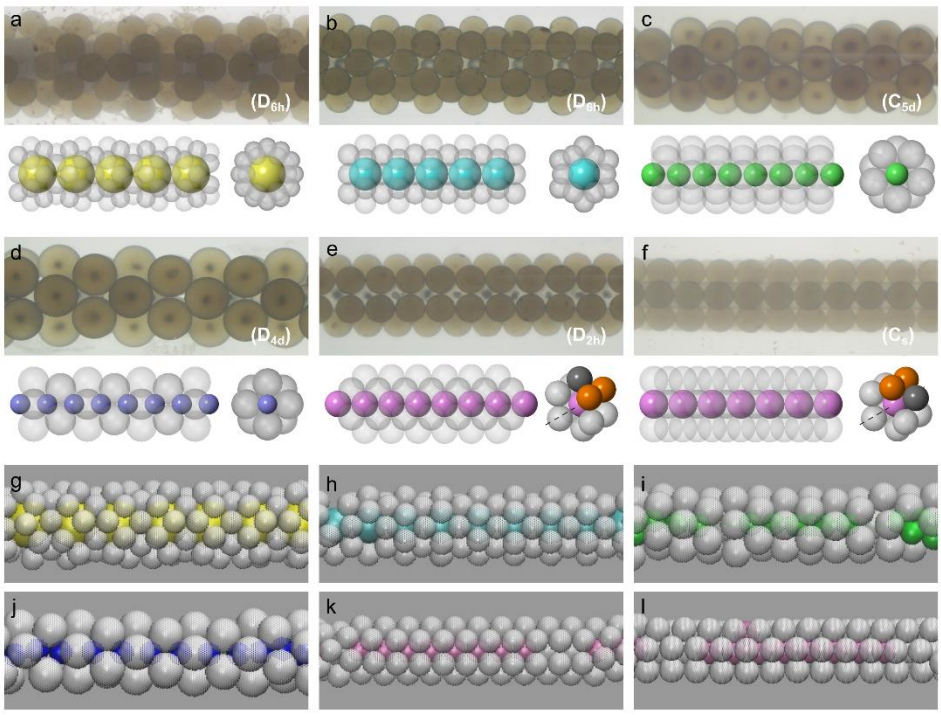

Figure 5. Multicomponent tubular packing. a–f) Cartoons below the experimental images illustrate the packing. The assemblies shown are for different ratios of particle sizes (d_{shell}/d_{core}) and particle

numbers (n_{core}:n_{shell}): a) 0.50 and 1:18, b) 0.67 and 1:12, c) 1.26 and 1:5, d) 1.50 and 1:4, e,f) 1 and 1:6. Point groups for each structure are also given. In the cartoon insets to (e) and (f), some shell spheres are colored in dark-gray and orange to illustrate how these particles are "interchanged" in the two polymorphs. The images in g–l) are structures reproduced in simulations (ω = 3000 rpm, L_{tube} = 75 mm, d_{tube} = 10 mm, ρ_l = 1.16 g cm^{-3}, $d_{particle}$ = 1.588–3.175 mm, $\rho_{light-particle}$ = 0.9 g cm^{-3}, $\rho_{dense-particle}$ = 1.13 g cm^{-3}).

2.6 Further demonstrations with immiscible liquids and bubbles

The experimental system described above can be extended to the assembly away from the axis of rotation. In particular, when immiscible liquids of different densities are rotated, they can form multilayer structures with concentric interfaces providing loci for the assembly of particles of different densities. The simplest, two-component system of this kind is shown in **Figure 6**a and comprises immiscible cesium bromide (ρ_1 = 1.07 g cm^{-3}, transparent, with 0.4 wt% Tween 80 surfactant) and oleic acid (ρ_2 = 0.887 g cm^{-3} < ρ_1, colored pink with oil red EGN dye) fluids. As in the classical spinning-droplet tensiometer (*31*), the lighter liquid is stretched and ultimately forms a cylinder along the axis of rotation. When 1 mm particles (green) with intermediate density $\rho_2 < \rho_{coll}$ = 1.021 g cm^{-3} < ρ_1 are present, they are pushed onto and organize at the cylindrical interface between the two fluids. Figure 6b show a more complex variant comprising three immiscible, rotating fluids–fluorinated liquid FC-40 (from 3M, ρ_1 = 1.855 g cm^{-3}, transparent), water with 0.4 wt% Tween 80 surfactant (ρ_2 ≈ 1.0 g cm^{-3} < ρ_1, colored orange with methyl orange), and oleic acid (ρ_3 = 0.887 g cm^{-3} < ρ_2, colored blue with Sudan blue II). When two types of particles of appropriately chosen densities are present, they separate and organize onto the two fluid–fluid interfaces – in Figure 6b, blue, 710 μm particles of density ρ_2 < ρ_{coll} = 1.13 g cm^{-3} < ρ_1 localize onto the outer cylindrical surface, while the white, 1 mm particles of density ρ_3 < ρ_{coll} = 0.96 g cm^{-3} < ρ_2 localize onto the inner cylindrical surface (outlined by dashed red lines in the left part of the image).

Last but not least, the "fluidic force fields" within rotating fluids can be used to control organization of deformable objects such as bubbles. Figure 6c has three snapshots illustrating the evolution of large air bubbles in poly(dimethylsiloxane) (PDMS). As the rotation rate is gradually increased from 0 to 5000 rpm over 300 s, the bubbles evolve from spherical to almost cylindrical. In the bottom picture, the boundaries between the bubbles are quite thin (<100 μm) and, interestingly, all disappear simultaneously when rotational speed is further increased. Another sequence of snapshots, for smaller bubbles, is illustrated in Figure 6d. Initially, there is a radial gradient of bubble sizes. Subsequently, the bubbles grow in size and assemble into cylindrical structures with at least some local helical ordering (in the bottom image, in region enclosed by yellow dashed lines). These and other bubble assemblies we prepared can be solidified suggesting possible uses as lightweight materials with mechanical

properties deriving from the particular distribution of bubbles of different sizes.

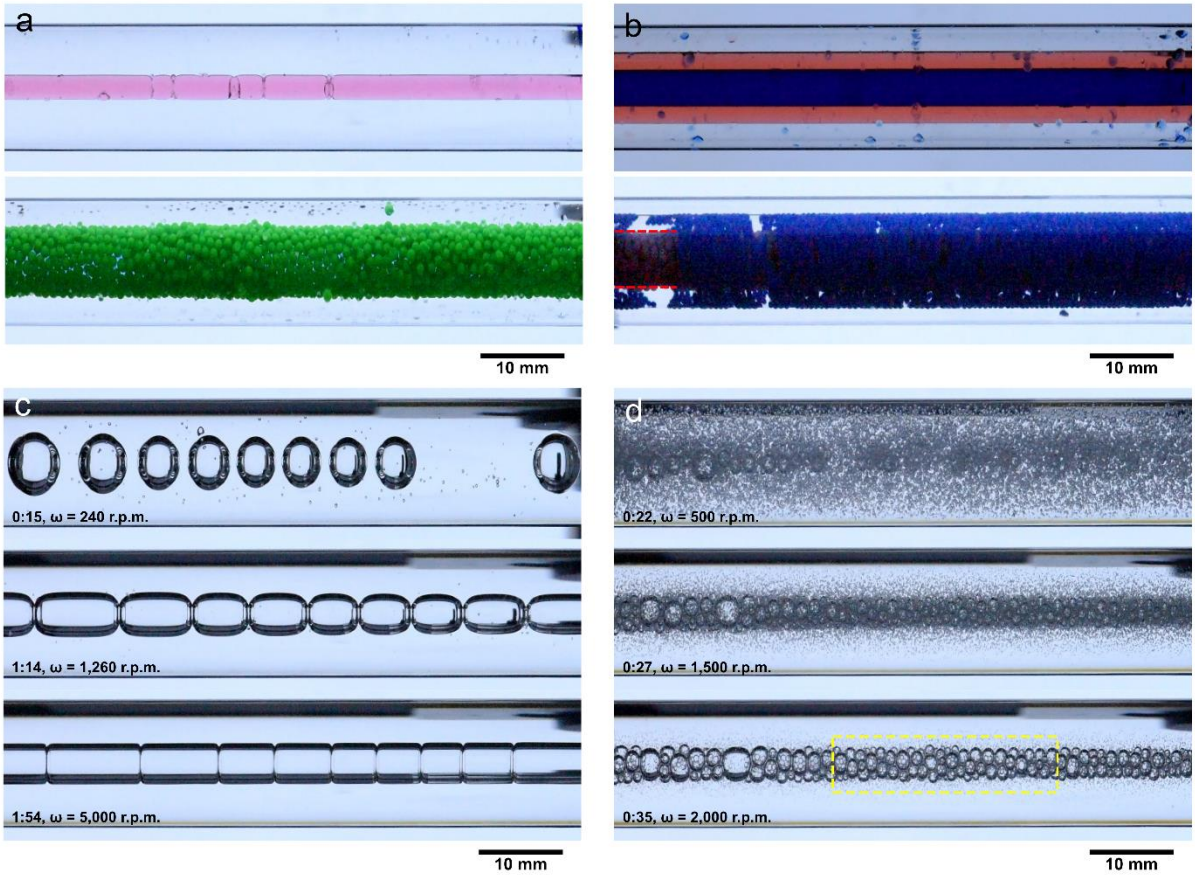

Figure 6. Extensions to the assembly on concentric interfaces and in ensembles of bubbles. a) Top: two immiscible fluids (cesium bromide solution with 0.4 wt% Tween 80 surfactant, transparent; oleic acid, pink) rotating at ω = 3000 rpm. Bottom: 1 mm particles (green) with intermediate density organize at the cylindrical interface between these two fluids (ω = 1800 rpm). b) An analogous system made of three immiscible fluids: fluorinated liquid FC-40 (transparent), water with 0.4 wt% Tween 80 surfactant (orange), and oleic acid (blue). Top: fluids rotating at 1400 rpm organize into concentric cylinders. Bottom: two types of particles separate and organize onto the two fluid–fluid interfaces at ω = 4000 rpm. c) Three snapshots illustrating the evolution of large air bubbles in PDMS. d) A similar sequence of snapshots of air bubbles in PDMS – the difference with (c) is that the bubbles are initially much smaller.

2.7 Summary

In summary, we have described an experimental system in which a denser fluid imposes a confining, cylindrically symmetric harmonic potential on lighter objects and thus drives formation of ordered, tubular structures near the axis of rotation or at concentric liquid–liquid interfaces. The main virtue of

this system is that the strength of confinement can be adjusted by the fluid's rate of rotation. In addition, lateral forces along the axis of rotation can be controlled by accelerating/decelerating the fluid, and we hypothesize that these forces can be further tuned by using tubes with nonuniform cross sections. We surmise that this modality of rotational self-assembly can prove useful in preparing composites (e.g., particles, bubbles, or maybe even cells in curable polymers or in gels) supporting radial gradients of composition and translating into a range of mechanical or optical properties of such fibrous structures.

References

[1] Airy, H. On Leaf-Arrangement. *Proc. R. Soc. Lond.* **1872**, *21*, 176-179.

[2] Adler, I.; Barabe, D.; Jean, R.V. A History of the Study of Phyllotaxis. *Ann. Bot.* **1997**, *80*, 231-244.

[3] Erickson, R.O. Tubular Packing of Spheres in Biological Fine Structure. *Science* **1973**, 181, 705-716.

[4] Pittet, N.; Boltenhagen, P.; Rivier, N.; Weaire, D. Structural Transitions in Ordered, Cylindrical Foams. *Europhys. Lett.* **1996**, *35*, 547-552.

[5] Hutzler, S.; Weaire, D.; Elias, F.; Janiaud, E. Juggling with Bubbles in Cylindrical Ferrofluid Foams. *Phil. Mag. Lett.* **2002**, *82*, 297-301.

[6] Tymczenko, M.; Marsal, L.F.; Trifonov, T.; Rodriguez, I.; Ramiro-Manzano, F.; Pallares, J.; Rodriguez, A.; Alcubilla, R.; Meseguer, F. Colloidal Crystal Wires. *Adv. Mater.* **2008**, *20*, 2315-2318.

[7] Li, F.; Badel, X.; Linnros, J.; Wiley, J.B. Fabrication of Colloidal Crystals with Tubular-like Packings. *J. Am. Chem. Soc.* **2005**, *127*, 3268-3269.

[8] Kohler, D.; Schneider, M.; Kruger, M.; Lehr, C.M.; Mohwald, H.; Wang, D.Y. Template-Assisted Polyelectrolyte Encapsulation of Nanoparticles into Dispersible, Hierarchically Nanostructured Microfibers. *Adv. Mater.* **2011**, *23*, 1376-1379.

[9] Mickelson, W.; Aloni, S.; Han, W.Q.; Cumings, J.; Zettl, A. Packing C_{60} in Boron Nitride Nanotubes. *Science* **2003**, *300*, 467-469.

[10] Warner, J.H.; Wilson, M. Elastic Distortions of Carbon Nanotubes Induced by Chiral Fullerene Chains. *ACS Nano* **2010**, *4*, 4011-4016.

[11] Yan, J.; Bloom, M.; Bae, S.C.; Luijten, E.; Granick, S. Linking Synchronization to Self-Assembly Using Magnetic Janus Colloids. *Nature* **2012**, *491*, 578-581.

[12] Zhou, Y.; Marson, R.L.; van Anders, G.; Zhu, J.; Ma, G.; Ercius, P.; Sun, K.; Yeom, B.; Glotzer, S.C.; Kotov, N.A. Biomimetic Hierarchical Assembly of Helical Supraparticles from Chiral Nanoparticles. *ACS Nano* **2016**, *10*, 3248-3256.

[13] Matthies, M.; Agarwal, N.P.; Schmidt, T.L. Design and Synthesis of Triangulated DNA Origami Trusses. *Nano Lett.* **2016**, *16*, 2108-2113.

[14] Adler, I. An Application of the Contact Pressure Model of Phyllotaxis to the Close Packing of

Spheres around a Cylinder in Biological Fine Structure. *J. Theor. Biol.* **1977**, *67*, 447-458.

[15] Pickett, G.T.; Gross, M.; Okuyama, H. Spontaneous Chirality in Simple Systems. *Phys. Rev. Lett.* **2000**, *85*, 3652-3655.

[16] Mughal, A.; Chan, H.K.; Weaire, D. Phyllotactic Description of Hard Sphere Packing in Cylindrical Channels. *Phys. Rev. Lett.* **2011**, *106*, 115704.

[17] Beller, D.A.; Nelson, D.R. Plastic Deformation of Tubular Crystals by Dislocation Glide *Phys. Rev. E* **2016**, *94*, 033004.

[18] Mann, S. Self-Assembly and Transformation of Hybrid Nano-Objects and Nanostructures under Equilibrium and Non-Equilibrium Conditions. *Nat. Mater*. **2009**, *8*, 781-792.

[19] Fialkowski, M.; Bishop, K.J.M.; Klajn, R.; Smoukov, S.K.; Campbell, C.J.; Grzybowski, B.A. Principles and Implementations of Dissipative (Dynamic) Self-Assembly. *J. Phys. Chem. B* **2006**, *110*, 2482-2496.

[20] Gizynski, K.; Lee, T.; Grzybowski, B.A. Dynamic Self-Assembly of Magnetic/Polymer Composites in Rotating Frames of Reference. *Adv. Mater.* **2017**, *29*, 1700614.

[21] Damasceno, P.F.; Engel, M.; Glotzer, S.C. Predictive Self-Assembly of Polyhedra into Complex Structures. *Science* **2012**, *337*, 453-457.

[22] Torquato, S.; Jiao, Y. Dense Packings of the Platonic and Archimedean Solids. *Nature* **2009**, *460*, 876-879.

[23] Mughal, A.; Chan, H.K.; Weaire, D.; Hutzler, S. Dense Packings of Spheres in Cylinders: Simulations. *Phys. Rev. E* **2012**, *85*, 051305.

[24] Fu, L.; Steinhardt, W.; Zhao, H.; Socolar, J.E.S.; Charbonneau, P. Hard Sphere Packing within Cylinders. *Soft Matter* **2016**, *12*, 2505-2514.

[25] Magnaudet, J.; Eames, I. The Motion of High-Reynolds-Number Bubbles in Inhomogeneous Flows. *Annu. Rev. Fluid Mech.* **2000**, *32*, 659-708.

[26] Bluemink, J.J.; Lohse, D.; Prosperetti, A.; van Wijngaarden, L. Drag and Lift Forces on Particles in a Rotating Flow. *J. Fluid Mech.* **2010**, *643*, 1-31.

[27] Batchelor, G.K. *An introduction to fluid dynamics*. Cambridge Univ. Press, 1967.

[28] Auton, T.R.; Hunt, J.C.R.; Prud'Homme, M. The Force Exerted on a Body in Inviscid Unsteady Non-Uniform Rotational Flow. *J. Fluid Mech.* **1988**, *197*, 241-257.

[29] Walton, O.R.; Braun, R.L. Viscosity, Granular-Temperature, and Stress Calculations for Shearing Assemblies of Inelastic, Frictional Disks. *J. Rheol.* **1986**, *30*, 949-980.

[30] COMSOL Multiphysics 5.1, COMSOL, Inc., Burlington, MA, USA.

[31] Princen, H.M.; Zia, I.; Mason, S.G. Measurement of Interfacial Tension from the Shape of a Rotating Drop. *J. Coll. Int. Sci.* **1967**, *23*, 99-107.

Appendix

When the rotating tubes were horizontal, we did not detect any preferred chirality of the helical assemblies that formed (**Figure A1** a,b). Lack of chiral selection was also confirmed in molecular dynamics simulations (Figure A1c) which we repeated 100 times, each time starting from random positions of beads. The ratio of right- to left-handed helices was 52:48.

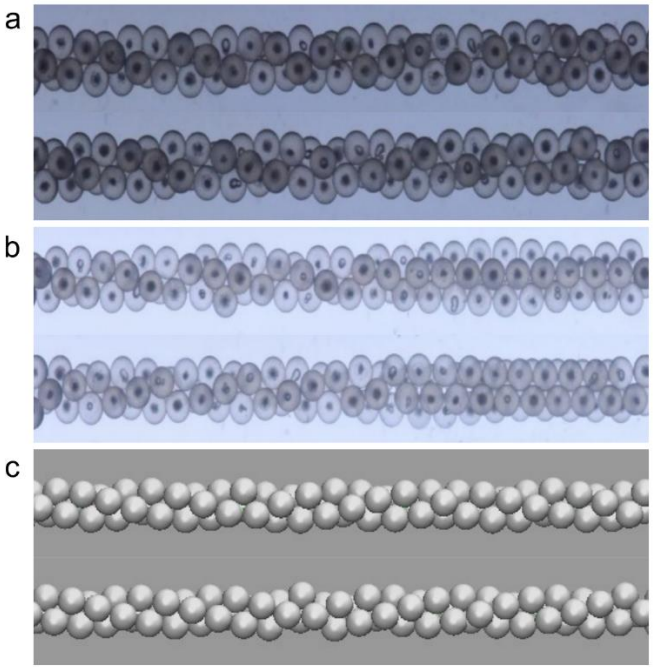

Figure A1. Lack of chiral selection for helical assemblies in (a,b) experiments and (c) simulations. Experimental examples in a,b are for, respectively, n/n_0 = 2.9, and n/n_0 = 3.2. c, Simulations were performed for n/n_0 = 3.2, L = 50 mm, ID_{tube} = 10 mm, d = 1.588 mm, ρ_l = 1.0 g cm^{-3}, ρ_p = 0.9 g cm^{-3}.

License for reusing the published paper (1/2)

JOHN WILEY AND SONS LICENSE
TERMS AND CONDITIONS

Nov 10, 2019

This Agreement between Ulsan National Institute of Science and Technology ("You") and John Wiley and Sons ("John Wiley and Sons") consists of your license details and the terms and conditions provided by John Wiley and Sons and Copyright Clearance Center.

License Number	4705290700520
License date	Nov 10, 2019
Licensed Content Publisher	John Wiley and Sons
Licensed Content Publication	Advanced Materials
Licensed Content Title	Non-Equilibrium Self-Assembly of Monocomponent and Multicomponent Tubular Structures in Rotating Fluids
Licensed Content Author	Bartosz A. Grzybowski, Konrad Gizynski, Taehoon Lee
Licensed Content Date	Nov 7, 2017
Licensed Content Volume	29
Licensed Content Issue	47
Licensed Content Pages	8

License for reusing the published paper (2/2)

Type of use	Dissertation/Thesis
Requestor type	Author of this Wiley article
Format	Print and electronic
Portion	Full article
Will you be translating?	No
Title of your thesis / dissertation	Dynamic Self-Assembly and 3D Fluidic Trap in Rotating Fluids
Expected completion date	Dec 2019
Expected size (number of pages)	80
Requestor Location	Ulsan National Institute of Science and Technology 50, UNIST-gil Ulsan 44919, Republic of Korea Ulsan, Ulsan 44919 Korea, Republic Of Attn: Ulsan National Institute of Science and Technology
Publisher Tax ID	EU826007151
Total	0.00 USD

Terms and Conditions

TERMS AND CONDITIONS

This copyrighted material is owned by or exclusively licensed to John Wiley & Sons, Inc. or one of its group companies (each a"Wiley Company") or handled

Chapter 3. Dynamic Assembly of Small Parts in Vortex-Vortex Traps Established within a Rotating Fluid.

3.1 Abstract

Stable, purely fluidic particle traps established by vortex flows induced within a rotating fluid are described. The traps can manipulate various types of small parts, dynamically assembling them into high-symmetry clusters, cages, interlocked architectures, jammed colloidal monoliths, or colloidal formations on gas bubbles. The strength and the shape of the trapping region can be controlled by the strengths of one or both vortices and/or by the system's global angular velocity. The system exhibits a range of interesting dynamical behaviors including a Hopf-bifurcation transition between equilibrium-point trapping and the so-called limit cycle in which the particles are confined to circular orbits. Theoretical considerations indicate that these vortex–vortex traps can be further miniaturized to manipulate objects with sizes down to ≈10 μm.

3.2 Introduction

The ability to trap and manipulate small objects in three dimensions—using either optical (*1–3*), magnetic (*4, 5*), acoustic (*6*), or dielectrophoretic fields (*7*) or microfluidic flows (*8, 9*)—has enabled applications ranging from atom-by-atom assembly (*10*), to Bose–Einstein condensation (*11*), to the manipulation of biomolecules (*12, 13*), colloids (*14*) and cells (*15*), to artificial insemination (*16, 17*), and more (*18, 19*). These methods differ in and are limited by the types and sizes of objects that can be manipulated—in particular, few can flexibly address and assemble larger nonmagnetic particles, from a tens of micrometers to millimeters, such as the components of mechanical systems or optical devices (*20, 21*), or tissue-like assemblies (*22, 23*). Here, we describe trapping in this regime of sizes enabled by vortex flows created within a rotating frame of reference. Although vortices and vortex systems (*24, 25*) typically do not create stable points within 3D flow fields, the situation changes when a pair of collinear vortices is generated within a fluid that is itself set on rigid-body rotation. Under these circumstances, the forces exerted by the vortices along the axis of rotation are accompanied by radially directed centripetal forces, in effect creating a region of strong trapping. Using this arrangement, we demonstrate trapping and dynamic assembly of various particle clusters, cages, and interlocked architectures, as well as jammed colloidal monoliths or colloidal formations on gas bubbles. In these experiments, the shape of the trapping region—and, consequently, the morphology of the assembling structures—can be controlled by adjusting the strengths of one or both vortices and/or the system's global angular velocity, and can switch from a stable equilibrium point to a limit cycle via the so-called supercritical Hopf bifurcation. These findings illustrate how new modalities of dynamic self-assembly (*26*) and 3D manipulation become possible upon transition from

static to noninertial, rotating frames of reference.

3.3 Particle trapping by collinear colliding vortices

When a lighter particle of volume V and density ρ_p is immersed in a rotating fluid of density $\rho_L > \rho_p$, it experiences not only an upward-directed buoyant force $\boldsymbol{F}_B = (\rho_p - \rho_L)\mathrm{V}\boldsymbol{g}$, but also a centripetal force directed toward the axis of tube's rotation, $\boldsymbol{F}_C(\boldsymbol{r}) = -(\rho_L - \rho_p)\mathrm{V}\boldsymbol{r}\omega^2$, where ω is fluid's angular velocity and vector $\boldsymbol{r}$ specifies particle's radial position (**Figure 1**a). In other words, the rotation of the tube imposes a confining harmonic potential, $\mathrm{E(r)} = (\rho_L - \rho_p)\mathrm{V}r^2\omega^2/2$. As we have shown previously (*27*), for polymer beads inside tubes ≈1 cm in diameter, filled with various aqueous salt solutions and rotating at few thousand rpm, centrifugal acceleration is on the order of $10g$ (allowing us to neglect buoyancy effects in the subsequent discussion), and the beads localize along the fluid's axis of rotation. On the other hand, radially directed forces do not displace the beads along the tube's rotation axis and cannot, by themselves, create a stable trapping region in the axial direction.

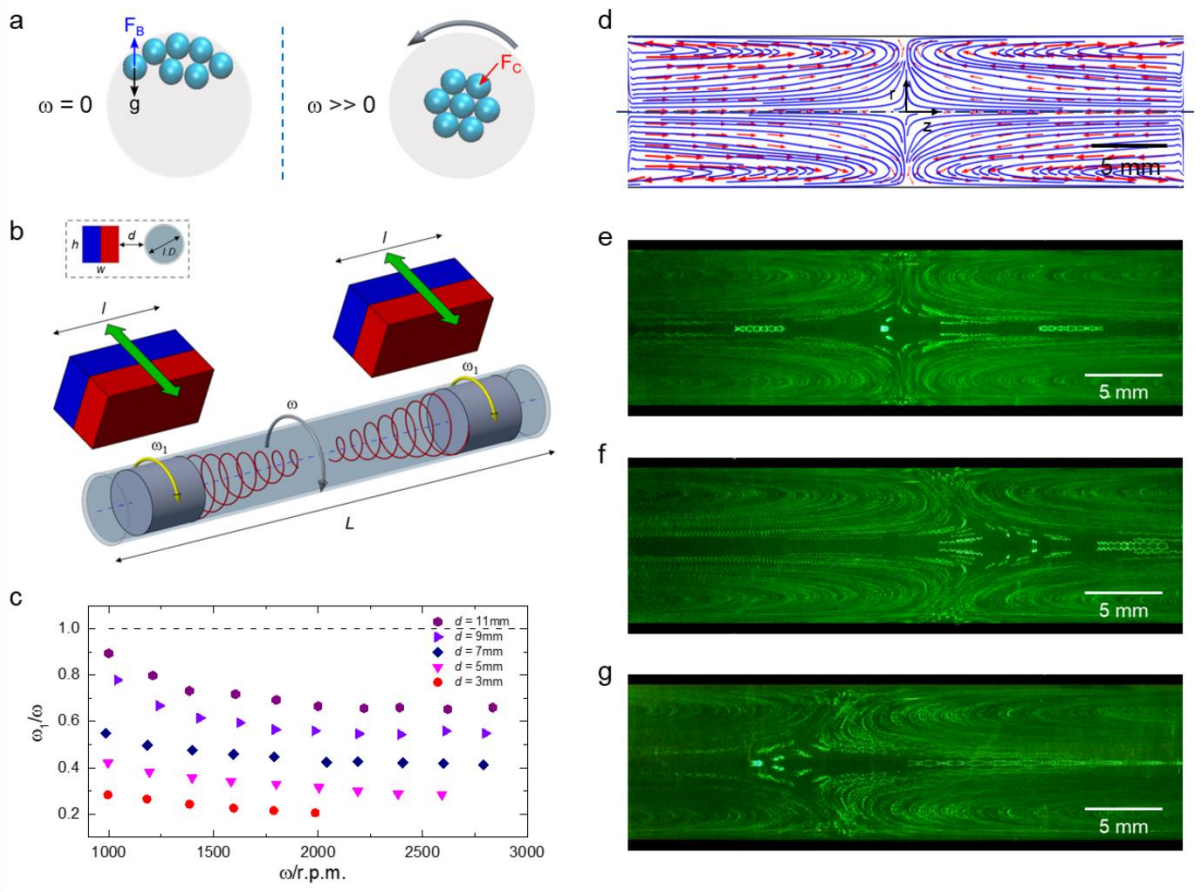

Figure 1. Experimental configuration of the vortex-vortex trapping system. a) Cross-sectional view of the tube housing lighter particles immersed in a denser liquid. When the tube rotates rapidly, the centripetal force, $\boldsymbol{F}_C$, directed towards the axis of rotation dominates buoyant force, $\boldsymbol{F}_B$. b) Scheme

of the experimental arrangement in which two aluminum disks inside of the tube are slowed down by externally-positioned permanent magnets (at variable distance *d*, see inset), effectively creating vortex flows in the liquid. c) Rotational velocity of the disks, ω_1, scales with but is smaller than that of the tube, ω. Different markers correspond to different distances, *d*, between the disks and magnets (see legend). The data was measured for a mixture of water and glycerol (78:22, w/w; $\rho_L =$ 1.05 g cm^{-3} and viscosity, 0.002 Pa s). Dashed line traces the $\omega_1/\omega = 1$ reference for which the disks are not retarded. d) Calculated velocity field of the flow and streamlines developed in the middle region of the tube. The calculations were performed in Comsol 5.1 for $d = 9$ mm and $\omega = 1500$ rpm. with fluid's properties used in (c) and the same velocities of both disks, $\omega_1 \sim 925$ rpm. e-g) Actual flow fields visualized by 10 μm fluorescent tracers in 25 wt% sucrose solution ($\rho_L = \sim 1.11$ g cm^{-3}). Panel (e) is for the case when both disks have similar angular velocities ($\omega_{1,left} \approx \omega_{1,right}$), and the vortices are symmetric. In panel (f), distance *d* is smaller for the left magnet-disk pair. Consequently, the left disk is slowed down more than the right one ($\omega_{1,left} < \omega_{1,right}$) and produces a stronger vortex reaching further to the right, beyond the midpoint of the tube. In panel (f), the opposite is true ($\omega_{1,left} > \omega_{1,right}$) and the right vortex is stronger.

To enable such lateral confinement, we designed a system (cf. Experimental system in Chapter 1.) in which two aluminum disks (radius 9.9 mm and thickness 16 mm) are fitted inside and near the two ends of the liquid-filled, rotating tube ≈1 cm in diameter. A permanent neodymium bar magnet (BX088-N52 from KJ Magnetics; $w = h = 12.5$ mm and $l = 25.4$ mm, magnetization along the *w* dimension = 588 mT) is placed at a distance *d* away from each disk (Figure 1b). The role of the magnets is to act as eddy-current brakes and slow down the rotation of the aluminum disks with respect to the rotation of the liquid-filled tube. Indeed, as the distance *d* between the disks and the magnets decreases, so does the disks' angular velocity, ω_1. For a given *d*, ω_1 increases with but is always smaller than the angular velocity of the tube, ω (Figure 1c). This slowed-down rotation of the disks gives rise to vortex flows inside of the tube (Figure 1b, d–g). The calculated and experimental images of the flow field due to the vortices are illustrated in Figure 1d–g—as seen, the flow has lateral components directed from each disk toward the center of the tube, diverges near the tube's center, and returns toward the disks along the tube's walls. Importantly, because the outward flows near the mid-plane are opposed by the radially confining harmonic potential (cf. above), we expect that for appreciably high rotation rates of the tube (imposing radial confinement) and for strong enough vortex flows (establishing lateral confinement), the central region can trap particles lighter than the fluid. We note that in experiments with very small particles, it is sometimes beneficial to place additional, tightly fitting rings between the disks and the central region with particles (cf. Figure 2a)—this prevents the small particles from getting stuck in the gaps between the disks and the tube and

jamming the former.

3.4 Ordered assembly and polymorph in 3D fluidic trap

Examples in **Figure 2** demonstrate that the system thus set up can act as a 3D fluidic trap. In Figure 2a, six spherical beads (diameter D = 250 μm; density, ρ_P = 0.98 g cm^{-3}) are placed in a cylindrical glass tube (ID = 10 mm; OD = 15 mm; length, L = 180 mm) filled with a mixture of water and glycerol (78:22, w/w; ρ_L = 1.05 g cm^{-3} and viscosity, 0.002 Pa s) and rotating at ω = 2200 rpm. When the flanking magnets are far away and the difference in the angular velocity of the tube and the aluminum disks is not very pronounced (i.e., $\omega_1/\omega \gtrsim 0.9$), the assembly is dominated by radial/centripetal forces and the beads align along the axis of rotation. When, however, the magnets are placed closer to the disks ($d \approx$ 11–13 mm) and slow them down perceptibly, vortex flows emerge and localize the beads to the mid-point of the tube, where they arrange into an octahedral cluster. Figure 2b,c shows full phase diagrams quantifying organization of n = 4 and n = 6 particles for various values of ω and d. The diagrams share several similarities for both n's. For instance, when d is small and the aluminum disks are markedly retarded, the strong vortices extend farther from the disks and give rise to swirling flows near mid-plane—consequently, the particles are not trapped to a stable, point-like region but exhibit orbiting trajectories in this plane (gray regions in the phase diagrams; also see discussion later in the text). In contrast, for large d (weak vortices) and large values of ω, the assemblies are dominated by centripetal forces and chain-up along the rotation axis. Trapping to a stable mid-point of the tube is observed for intermediate d and ω values—we note that for n = 4, only one type of a cluster (tetrahedral) is observed (green region in Figure 2b) but for n = 6, there are two polymorphs, octahedral and pentagonal-pyramid clusters (in Figure 2c, green and blue regions, respectively).

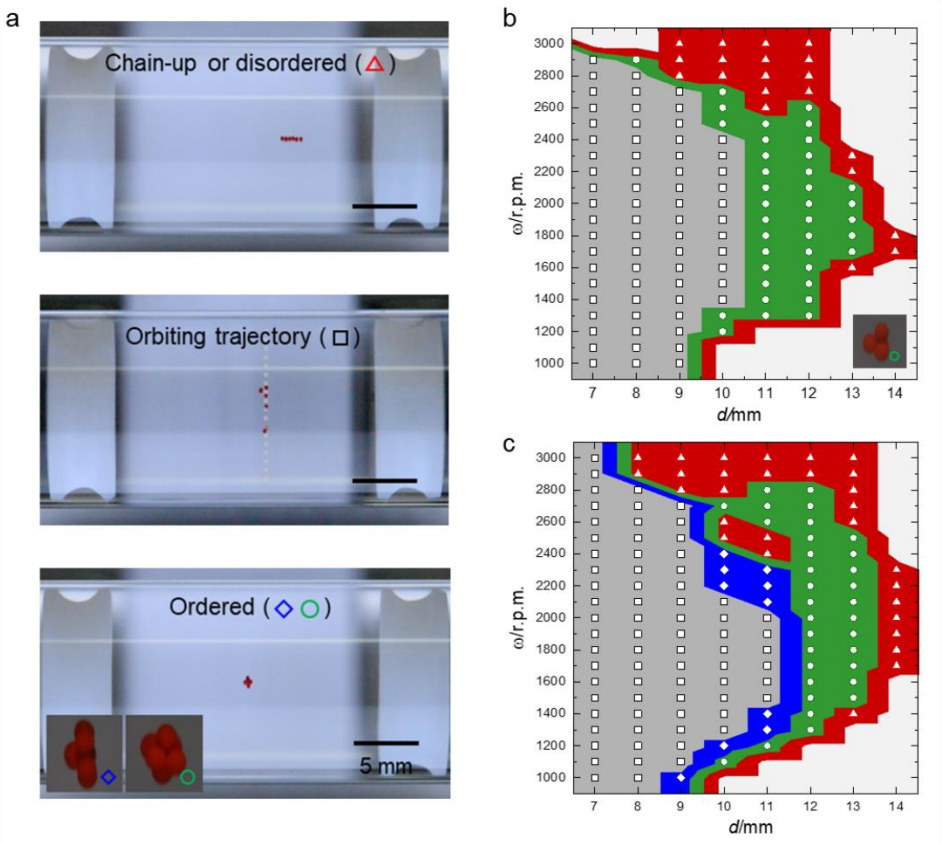

Figure 2. Trapping of particle clusters and phase diagrams. a) Three predominant modes of organization illustrated here for six D = 250 μm particles: top) linear assembly along the axis of rotation; middle) particles orbiting along the tube's mid-plane; bottom) stable particle clusters in the trapping region (insets show two possible polymorphs). In the photographs, notice white, tightly fitting plastic rings inserted into the tube to prevent the small particles from jamming the aluminum disks (though, if disks are made to fit the tube relatively tightly, such disks are not necessary). Phase diagrams for systems of b) n = 4 and c) n = 6 of 250 μm particles. Phases are denoted by different markers corresponding to the images in (a). The markers indicate experimental results and the color map is drawn by interpolating the data. Unmarked/white regions represent cases where the particles' dynamics cannot be easily determined/classified (e.g., when the particles collide with the disks; also see Appendix).

Polymorphs are also observed for some other particle numbers (e.g., n = 5, 7, 9, and 10 but not for n = 8; **Figure 3**a; also see Figure A1a in Appendix). Perhaps the most interesting case is for n = 13 which is relevant to the centuries-old mathematical problem of the kissing number—that is, how many hard spheres can surround and touch a common central sphere. Although the problem dates back to Newton, it was only in 1953 that it was formally proven that in 3D, the maximum kissing number is 12, with the possibility to arrange outer spheres in infinitely many configurations (*28*, *29*). Our

experimental system not only realizes several such configurations but, by changing particle densities, allows for the selection of the most dominant polymorph. For instance, for all identical spheres (e.g., in Figure 3b, D = 500 μm, ρ_P = 1.13 g cm^{-3}, ρ_L = 1.15 g cm^{-3}, ω = 750–1250 rpm, d = 6–8 mm), the fcc-packed structure is most frequently observed and remains stable over a relatively wide range of parameters ($\Delta d \approx$ 1.5 mm). An icosahedral packing is less frequent and less stable (only within $\Delta d \leq$ 0.3 mm) and so is the modified icosahedral packing in which the two five-sphere rings surrounding the three (core) spheres are slightly further apart. Interestingly, despite this small difference, the icosahedral and icosahedral-like structures are readily distinguishable because they are differently oriented with respect to the rotation axis (since the harmonic confining potential strives to minimize the cluster's moment of inertia with respect to the tube's axis of rotation; Figure 3c). Now, when one blue particle is replaced by a lighter (ρ_P = 0.98 g cm^{-3}) red sphere of the same size, this sphere—experiencing largest confining force—localizes preferentially to the cluster's center and the icosahedral packing becomes dominant (Figure 3d), with the other two being observed only sporadically. When three lighter spheres are used, they align along the axis of tube's rotation, completely eliminating formation of the fcc structure (Figure 3e).

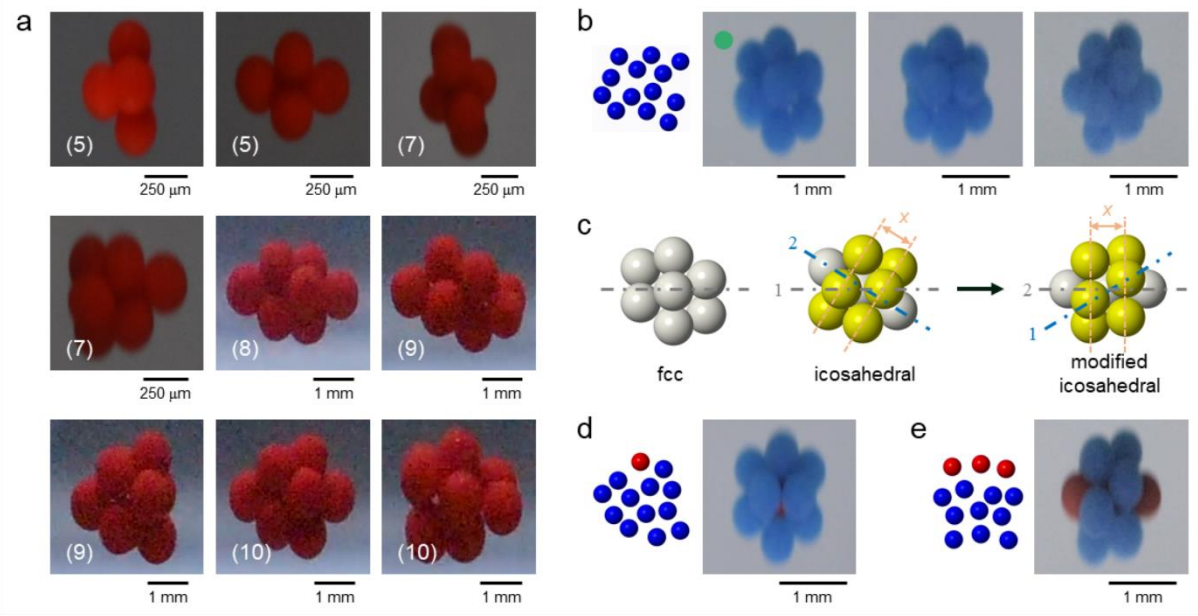

Figure 3. Examples of polymorphic particle clusters. a) Clusters formed by n = 5–10 particles (numbers of particles are in the parentheses). Polymorphs are not observed only for n = 8. For n = 5 and 7, the sizes of particles are 250 μm (ρ_P = 0.98 g cm^{-3}) and the solution is a mixture of water and glycerol (ρ_L = 1.05 g cm^{-3}). The ordered clusters were obtained at ω = 1500–2500 rpm. and d = 10–13 mm. For n = 8–10, we used 1 mm particles (ρ_P = 0.98 g cm^{-3}) and CsBr solution (ρ_L = 1.2 g cm^{-3}) and obtained those clusters at ω = 3500–4500 rpm. and d = 2–4 mm. b) Polymorphs formed by n = 13 identical D = 500 μm spheres. The structures are fcc, icosahedral, and modified icosahedral packings

(from left to right). Green marker indicates dominant packing. c) Cartoons of the three distinct packings. For each packing, the principal axis is indicated by a grey dash-dot line. The icosahedral and modified icosahedral packings (which look very similar but differ in the distance *x* between the outer rings of yellow-colored particles) can be distinguished by the rotation axis; "1" for the former and "2" for the latter. Experimental images of packings observed for systems consisting of d) 1 red and 12 blue spheres, and e) 3 red and 10 blue spheres. The red spheres (ρ_P = 0.98 g cm^{-3}) are lighter than the blue ones (ρ_P = 1.13 g cm^{-3}) and preferentially localize onto the axis of rotation. For 13-sphere packings, we used a mixture of 4.1M NaCl solution and glycerol (8/2, v/v; ρ_L = 1.15 g cm^{-3}).

3.5 Various assemblies by non-spherical particles and particles' jamming

A rich variety of trapped structures can be observed with components having different sizes and/or nonspherical shapes. For instance, smaller spheres can form centrally positioned rings around larger spheres (**Figure 4**a) or bubbles (Figure 4b). Polygonal plates can be assembled into boxes around spherical particles (Figure 4c,d), whereas rings can be threaded onto rods (Figure 4e). In these experiments, the fidelity of assembly into perfectly ordered structures decreases with the number of the same-type particles present (as expected for glass-forming systems), and is also problematic with plate-like parts that tend to stack-up (e.g., in the box structures around spheres whereby, in the majority of cases, not all faces are "closed"; see Figure 4c,d; for failure modes of these structures, also see Figure A1b–d in Appendix). Another interesting situation arises when a cluster that forms consists of large numbers of small particles, assuming its changing shape. Under these circumstances, the varying degrees of confinement can control particles' jamming. For example, in **Figure 5**a, the collection of D = 50 μm, ρ_P = 0.98 g cm^{-3} particles is subject to only moderate radial confinement (ω = 800 rpm) and when the lateral, confining vortex flows become stronger—upon decreasing the distance to the magnets, d, from 20 to 9 mm—the agglomerate gradually evolves from an oblong ellipsoid to a roughly spherical formation. In contrast, when the vortices act on particles subject to stronger radial confinement, ω = 1800 rpm, they are jamming and cannot relax to the spherical shape. Instead, the formation changes from a dumbbell to a cylindrical shape (Figure 5b). Finally, we note that in these and other experiments we described, the trap can be made laterally asymmetric by using unequal distances of the magnets to proximal aluminum disks, thus individually adjusting vortex strengths. For instance, Figure 5c shows a half-ellipsoid assembly of 50 μm particles observed when the confining vortex acting from one direction is much stronger than that acting from the other (distances to the magnets d_{left} = 8 mm vs d_{right} = 12 mm). Another example of an asymmetric shape is shown in Figure 5d illustrating time evolution and relaxation with time.

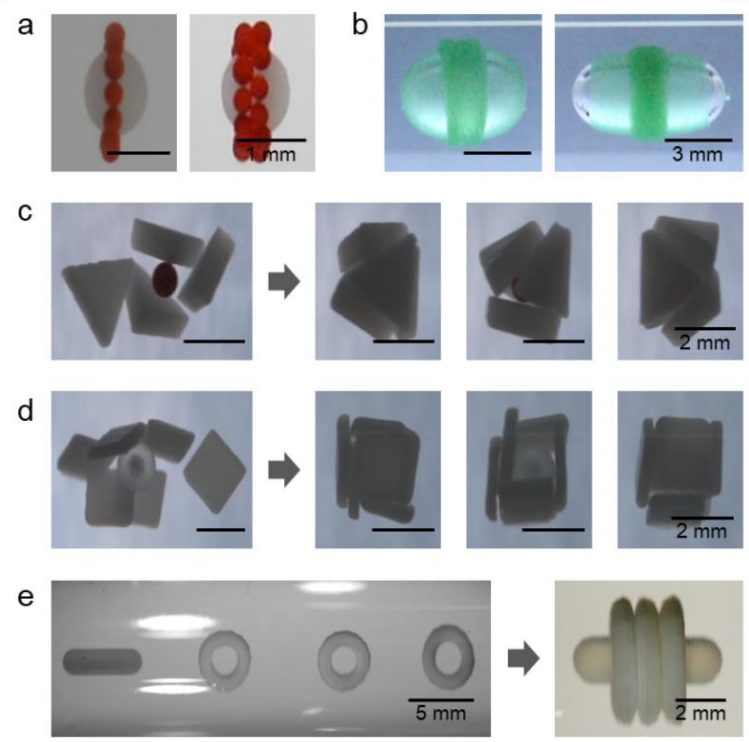

Figure 4. Examples of trapped structures assembled from non-identical components. a) Binary structures with a single chain of 13 spheres (*left*) and double chain of 25 spheres (*right*) surrounding one large sphere. The diameters of spheres are 250 µm for the red ones (ρ_P = 0.98 g cm^{-3}) and 1 mm for the white one (ρ_P = 0.96 g cm^{-3}). Here, mixtures of water/glycerol (78/22, w/w; ρ_L = 1.05 g cm^{-3}) and 2M NaCl/glycerol (8/2, v/v; ρ_L = 1.1 g cm^{-3}) were used for single- and double-chain structures, respectively. b) Colloids on air bubbles. 50 µm particles form a band around a centrally positioned air bubble in a solution of water/EG (5/5, v/v; ρ_L = 1.06 g cm^{-3}). As the radial confining force increases from ω = 2000 rpm (*left*) to 3000 rpm. (*right*), the particles are more concentrated in the band and the bubble becomes more elliptic. Self-assembly of c) tetrahedral and d) cubic "cages". In (c), four triangular plates (edge length, a = 2 mm; ρ_P = 1.02 g cm^{-3}) assemble into a "box" surrounding a central, D = 800 µm sphere (ρ_P = 0.98 g cm^{-3}). In the box in (d), two square plates (a = 1.88 mm, ρ_P = 1.02 g cm^{-3}) are stacked so the box has one face open, exposing the inner, D = 1.6 mm sphere (ρ_P = 0.9 g cm^{-3}). e) An interlocked, "rotaxane" structure assembled from one rod (D = 1.5 mm, L = 6 mm, ρ_P = 1.02 g cm^{-3}) and three rings (D_{inner} = 2 mm, D_{outer} = 4 mm, ρ_P = 1.02 g cm^{-3}). The initial configuration of the components is essential for the formation of this assembly; the rod should not be placed between the rings or else disordered structures form, see also Figure A1d in Appendix. In (c)–(e), the plates, cylinders, and rings were fabricated via 3D printing and the solution was a mixture of fluorinated liquid (3M Novec 7200 Engineered Fluid) and silicone oil (PDMS, viscosity 10 cSt, Sigma Aldrich) in a 7/3 v/v ratio and density, ~1.3 g cm^{-3}.

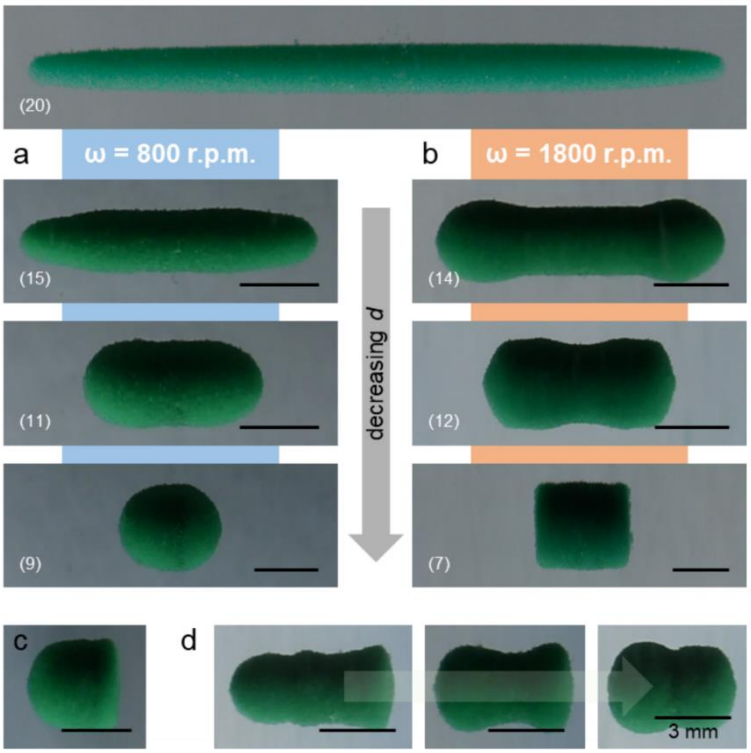

Figure 5. Particle's jamming and asymmetric assemblies. a) Gradual transformation—from an oblong ellipsoid to approximately a sphere—of a formation of large numbers of small particles. The top panel shows a structure at large *d* (=20 mm) from which we studied morphological changes by sequentially decreasing *d*. Specific values of *d* in mm are given by white-font numbers in parentheses. b) "Jammed" transformation at increased radial confinement. In contrast to (a), stronger radial confinement prevents the assembly from relaxing to the spherical shape, instead, the monolith evolves from a dumbbell to a cylinder. The experiment is for 1800 rpm, but the effects of confinement become manifest already at 1200 rpm. c) Asymmetric assembly driven by disks rotating at different rates and creating vortices of different strengths. In this example, ω_{tube} = 1500 rpm and $\omega_{1,left} < \omega_{1,right}$. d) Time evolution of an asymmetric colloidal assembly (ω_{tube} = 1400 rpm and $\omega_{1,left} < \omega_{1,right}$). The arrow indicates passage of time, spanning a period of about an hour. In all experiments, the particles were 50 μm in diameter, had a density of 0.98 g cm^{-3}, and the solution was a mixture of fluorinated liquid (3M Novec 7200 Engineered Fluid) and silicone oil (PDMS, viscosity 10 cSt, Sigma Aldrich) in a 3/7 v/v ratio and density ≈1.08 g cm^{-3}. All scale bars are 3 mm.

3.6 Theoretical study of fluidic trap and Hopf bifurcation

The properties of our vortex–vortex traps merit additional theoretical discussion. In general, the ability to trap particles derives from an interplay between centripetal forces, $\boldsymbol{F}_C = -(\rho_L - \rho_P)V\boldsymbol{r}\omega^2$ and the forces imparted on the particles by the vortices. A simplified yet realistic model—capturing most of trap's characteristics—considers the drag forces the particles experience in vortex flows,

$\boldsymbol{F}_{vort} = 3\pi\eta D\boldsymbol{u}$ where η is viscosity of the fluid, D is particle's diameter, and $\boldsymbol{u}$ is fluid's velocity calculated numerically (ref. *30* and Figure 1d) for an axisymmetric geometry and with boundary conditions at the surfaces of the slowed-down disks obtained from their experimentally measured angular velocities (see Figure 1c). With these assumptions, we consider the radial, r, and axial, z, components of $\boldsymbol{F}_C(\boldsymbol{r}) + \boldsymbol{F}_{vort}$ to delineate the regions of trap's stability for a particle of certain diameter. Maps in **Figure 6**a are (r, z) cross-sections near the rotating tube's center (−5 mm < r < 5 mm, −2 mm < z < 2 mm) for D = 100 μm particles (ρ_P = 0.98 g cm^{-3}, ρ_L = 1.05 g cm^{-3}, η = 0.002 Pa s, and ω = 2000 rpm) and vortex strength decreasing from left to right (d increasing from 3 to 11 mm). A particle is only attracted into regions where $|\boldsymbol{F}| = 0$, and $\frac{\partial F_z}{\partial z} < 0$ and $\frac{\partial F_r}{\partial r} < 0$. Since pinpointing locations where $|\boldsymbol{F}| = 0$ is complicated by finite precision of numerically calculated flow fields, we highlight contours (white) where $|\boldsymbol{F}|$ is equal to some small value (say, 0.1 nN) such that the zero-force, equilibrium point is contained somewhere within the contour. Blue color indicates regions over which $\frac{\partial F_z}{\partial z} < 0$ and $\frac{\partial F_r}{\partial r} < 0$, which makes zero-force points there stable (if any); green color delineates regions where $\frac{\partial F_z}{\partial z} > 0$ or $\frac{\partial F_r}{\partial r} > 0$, so even zero-force point in these regions would be unstable. At d = 3 mm, the on-axis zero-force point is unstable ($\frac{\partial F_r}{\partial r} > 0$), and the only stable zero-force points are off the axis. Given that the model is axisymmetric, these two points correspond to a ring trajectory along the mid-plane of the tube—indeed, for strong lateral confinement, we see such trajectories in experiment (cf. Figure 2a–c and gray regions in the phase maps therein). For $d \geq 5$ mm, the stable equilibrium point localizes onto the axis of rotation enabling trapping and assembly of 3D structures. As seen, when d increases, the shape of the trap changes from an oblate spheroid ($F_z > F_r$), to a sphere ($F_z \approx F_r$), to a prolate spheroid ($F_z < F_r$), which is again in agreement with our experimental observations (cf. Figure 5a). These characteristics of the trap are summarized in Figure 6b in which the pink contour traces the region of parameter space for which the trap is approximately isotropic (spherical).

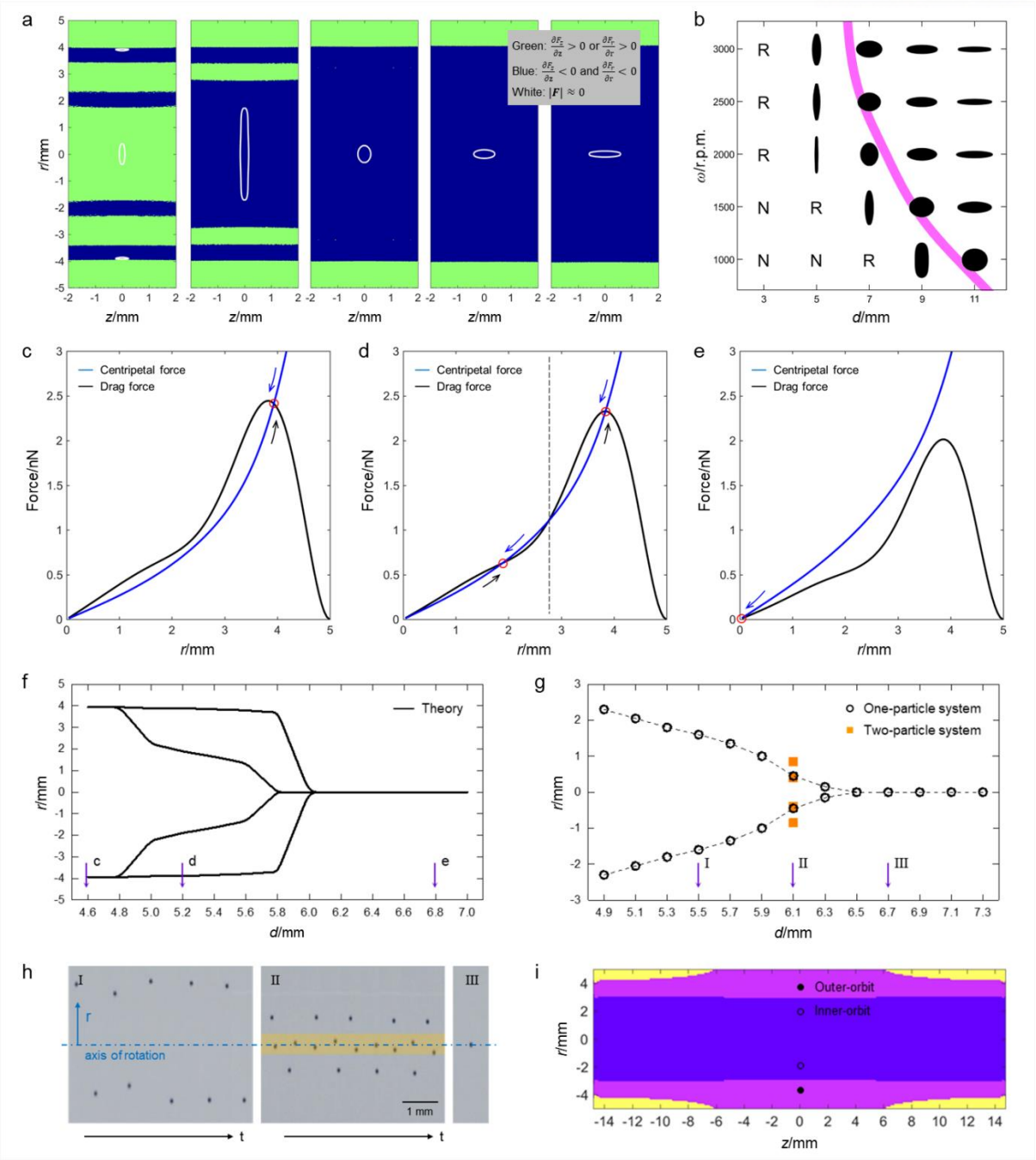

Figure 6. Theoretical studies of the vortex-vortex trap and Hopf bifurcation. a) Partial derivatives of force field (color map) and near-zero-force lines (white) for 100 μm particle system at ω = 2000 rpm and d = 3, 5, 7, 9, and 11 mm (from left to right). b) Various contours of the trapping region for 100 μm particle as a function of ω and d. Here, letter N denotes no-particle-trapping and R indicates a ring trajectory in the mid-plane of the tube. Regions for an isotropic shape of the trap (pink) were estimated by interpolating the simulation results. Confining force curves for states of c) a limit cycle (d = 4.6 mm), d) two limit cycles (d = 5.2 mm), and e) a stable equilibrium (d = 6.8 mm) at the mid-plane of the tube (z = 0) and plotted along the radial coordinate, r. The red circles indicate stable

equilibrium positions of a particle at given conditions. The arrows and the dotted line are inserted to illustrate particle trapping. Stability maps of 100 μm particle system obtained from f) theoretical model and g) experiment. Theoretical model predicts the existence of two limit cycles at $4.8 < d < 6.0$. In the experiment, two limit cycles were observed only in a system of two particles; these two limit cycles converged into one limit cycle with a small change of distance, d (Δd = 0.2 mm). In (f) and (g), the arrows indicate the values of d at which data are used for (c)–(e) and (h). h) Experimental images for states of a limit cycle (I, d = 5.5 mm), two limit cycles (II, d = 6.1 mm), and a stable equilibrium (III, d = 6.7 mm). Colored region in the middle image (II) marks a smaller limit cycle. i) Basin of attraction for the two limit cycles. Basins of attraction for inner and outer orbits are distinguished by different colors. Here, the condition for calculation corresponds to that of (d). In (c)–(i), the rotational rate of the tube is 1800 rpm.

We note that the transition between particle's ring orbit ("limit cycle") and a stable trapping point ("stable equilibrium") upon the change in single parameter d proceeds without hysteresis (cf. Figure A2 in Appendix) and is a manifestation of the so-called supercritical Hopf bifurcation well known in the mathematical theory of dynamical systems (*31*). This is corroborated by Figure 6c–e plotting the centripetal force (directed towards the axis of rotation) and the drag force (directed away from this axis) at the mid-plane of the rotating tube for three different values of d and with other parameters held constant (D = 100 μm, ω = 1800 rpm, $\rho_L - \rho_P$ = 0.06 g cm^{-3}, η = 0.002 Pa s); the stable points are marked by red circles. Interestingly, the model predicts not only the Hopf bifurcation but also the existence of two limit cycles for intermediate values of d (Figure 6d,f). We actually verified this prediction experimentally for the system of polystyrene particles (D = 100 μm, ρ_P = ~ 1.05 g cm^{-3}) in 25 wt% sucrose solution (ρ_L = ~ 1.11 g cm^{-3}) rotating at ω = 1800 rpm and d = 4.9–7.3 mm (Figure 6g,h). When just one particle was used, it always located to one, inner orbit. However, with two particles present and $d \approx 6.1$ mm, the second particle occupied the larger-radius, outer orbit as illustrated in experimental images in Figure 6h. The relatively narrow range of parameters for which two orbits are occupied can be reasonably attributed to the fact that the inner-orbit limit cycle has a larger basin of attraction than the outer-orbit one (Figure 6i).

3.7 Estimation of a lower limit of particle size in the trap

Finally, we note that a theoretical model described in Appendix indicates that the lower limit for the size of a particle that can be trapped scales as $R^2 \approx \frac{C}{\omega^2}\left(\frac{(\omega-\omega_1)}{\omega} + 3\frac{(\omega-\omega_1)^2}{\omega^2}\right)$, where $C = \frac{9K\eta^2}{4(\rho_L-\rho_P)\rho_L H^2}$, in which H is the distance between the aluminum disks, and K is the dimensionless factor that depends on the ratio of H and the tube's inner diameter. Using this model, we estimate

that at higher rotational rates (not available in our current set-up for technical and safety reasons), the traps can be effective for particles with sizes down to ca. 10 μm. For example, for ω = 10,000 rpm., ω_1 = 400 rpm, η = 2.175 mPa s, ρ_L = 1.104 g cm^{-3}, ρ_P = 0.98 g cm^{-3}, ID = 10 mm, H = 30 mm, one should be able to trap particles of ~6 μm radii.

3.8 Summary

In summary, we showed that by embedding vortex flows inside a rotating frame of reference, it is possible to realize purely fluidic 3D traps. Although theory suggests these traps can be further miniaturized and can potentially address singe cells or colloids, the current experimental setup is limited to larger particles (> tens of μm), which is the size regime relevant to the manipulation and assembly of small-part mechanical systems and also of certain biological specimens, such as cell spheroids (*32*) important in cell biology (and potentially benefitting from "clean," substrate-free positioning subject to spatially variable forces our system readily offers). We envision that for the assembly of small parts, it will be important to solidify the dynamic structures that form in the trap, perhaps by using liquid-solder methods (*33*, *34*). Last but not least, the traps exhibit a range of interesting non-linear behaviors, including bifurcations, suggesting they can be used as test-beds for studying various dynamical systems comprised of differently sized and/or shaped particles.

References

[1] Ashkin, A. Acceleration and Trapping of Particles by Radiation Pressure. *Phys. Rev. Lett.* **1970**, *24*, 156-159.

[2] Ashkin, A.; Dziedzic, J. M. Optical Trapping and Manipulation of Viruses and Bacteria. *Science* **1987**, *235*, 1517-1520.

[3] Raab, E. L.; Prentiss, M.; Cable, A.; Chu, S.; Pritchard, D. E. Trapping of Neutral Sodium Atoms with Radiation Pressure. *Phys. Rev. Lett.* **1987**, *59*, 2631-2634.

[4] Strick, T. R.; Allemand, J.-F.; Bensimon, D.; Bensimon, A.; Croquette, V. The Elasticity of a Single Supercoiled DNA Molecule. *Science* **1996**, *271*, 1835-1837.

[5] Timonen, J. V.; Grzybowski, B. A. Tweezing of Magnetic and Non-Magnetic Objects with Magnetic Fields. *Adv. Mater* **2017**, *29*, 1603516.

[6] Marzo, A.; Seah, S. A.; Drinkwater, B. W.; Sahoo, D. R.; Long, B.; Subramanian, S. Holographic Acoustic Elements for Manipulation of Levitated Objects. *Nat. Commun.* **2015**, *6*, 8661.

[7] Zhang, C.; Khoshmanesh, K.; Mitchell, A.; Kalantar-zadeh, K. Dielectrophoresis for Manipulation of Micro/Nano Particles in Microfluidic Systems. *Anal. Bioanal. Chem.* **2010**, *396*, 401-420.

[8] Sundararajan, N.; Pio, M. S.; Lee, L. P.; Berlin, A. A. Three-Dimensional Hydrodynamic Focusing in Polydimethylsiloxane (PDMS) Microchannels. *J. Micro-mech. Syst.* **2004**, *13*, 559-567.

[9] Karimi, A.; Yazdi, S.; Ardekani, A. M. Hydrodynamic Mechanisms of Cell and Particle Trapping in Microfluidics. *Biomicrofluidics* **2013**, *7*, 021501.

[10] Barredo, D.; Lienhard, V.; de Léséleuc, S.; Lahaye, T.; Browaeys, A. Synthetic Three-Dimensional Atomic Structures Assembled Atom by Atom. *Nature* **2018**, *561*, 79-82.

[11] Anderson, M. H.; Ensher, J. R.; Matthews, M. R.; Wieman, C. E.; Cornell, E. A. Observation of Bose-Einstein Condensation in a Dilute Atomic Vapor. *Science* **1995**, *269*, 198-201.

[12] Wang, M. D.; Yin, H.; Landick, R.; Gelles, J.; Block, S. M. Stretching DNA with Optical Tweezers. *Biophys. J.* **1997**, *72*, 1335-1346.

[13] de Vries, A. H. B.; Krenn, B. E.; van Driel, R.; Subramaniam, V.; Kanger, J. S. Direct Observation of Nanomechanical Properties of Chromatin in Living Cells. *Nano Lett.* **2007**, *7*, 1424-1427.

[14] Li, T.; Kheifets, S.; Medellin, D.; Raizen, M. G. Measurement of the Instantaneous Velocity of a Brownian Particle. *Science* **2010**, *328*, 1673-1675.

[15] Lin, L.; Peng, X.; Wei, X.; Mao, Z.; Xie, C.; Zheng, Y. Thermophoretic Tweezers for Low-Power and Versatile Manipulation of Biological Cells. *ACS Nano* **2017**, *11*, 3147-3154.

[16] Nascimento, J. M.; Shi, L. Z.; Meyers, S.; Gagneux, P.; Loskutoff, N. M.; Botvinick, E. L.; Berns, M. W. The Use of Optical Tweezers to Study Sperm Competition and Motility in Primates. *J. Roy. Soc.*

Interface **2008**, *5*, 297-302.

[17] Hyun, N.; Chandsawangbhuwana, C.; Zhu, Q.; Shi, L. Z.; Yang-Wong, C.; Berns, M. W. Effects of Viscosity on Sperm Motility Studied with Optical Tweezers. *J. Biomed. Opt.* **2012**, *17*, 025005.

[18] Jamshidi, A.; Pauzauskie, P. J.; Schuck, P. J.; Ohta, A. T.; Chiou, P.-Y.; Chou, J.; Yang, P.; Wu, M. C. Dynamic Manipulation and Separation of Individual Semiconducting and Metallic Nanowires. *Nat. Photon.* **2008**, *2*, 86-89.

[19] Friddin, M. S.; Bolognesi, G.; Elani, Y.; Brooks, N. J.; Law, R. V.; Seddon, J. M.; Neil, M. A. A.; Ces, O. Optically Assembled Droplet Interface Bilayer (OptiDIB) Networks from Cell-Sized Microdroplets. *Soft Matter* **2016**, *12*, 7731-7734.

[20] Subramaniam, A. B.; Yang, D.; Yu, H-D.; Nemiroski, A.; Tricard, S.; Ellerbee, A. K.; Soh, S.; Whitesides, G. M. Noncontact Orientation of Objects in Three-Dimensional Space Using Magnetic Levitation. *Proc. Natl. Acad. Sci. USA* **2014**, *111*, 12980-12985.

[21] Mirica, K. A.; Ilievski, F.; Ellerbee, A. K.; Shevkoplyas, S. S.; Whitesides, G. M. Using Magnetic Levitation for Three Dimensional Self-Assembly. *Adv. Mater.* **2011**, *23*, 4134-4140.

[22] Parfenov, V. A.; Koudan, E. V.; Bulanova, F. A.; Karalkin, P. A.; Pereira, F. D.A.S.; Norkin, N. E.; Knyazeva, A. D.; Gryadunova, A. A.; Petrov, O. F.; Vasiliev, M. M.; Myasnikov, M. I.; Chernikov, V. P.; Kasyanov, V. A.; Marchenkov, A. Y.; Brakke, K.; Khesuani, Y. D.; Demirici, U.; Mironov, V. A. Scaffold-Free, Label-Free and Nozzle-Free Biofabrication Technology Using Magnetic Levitational Assembly. *Biofabrication* **2018**, *10*, 034104.

[23] Timonen, J. V. I.; Raimondo, C.; Pilans, D.; Pillai, P. P.; Grzybowski, B. A. Trapping, Manipulation, and Crystallization of Live Cells Using Magnetofluidic Tweezers. *Nanoscale Horiz.* **2017**, ***2***, 50-54.

[24] Grzybowski, B. A.; Stone, H. A.; Whitesides, G. M. Dynamic Self-Assembly of Magnetized, Millimetre-Sized Objects Rotating at a Liquid–Air Interface. *Nature* **2000**, *405*, 1033-1036.

[25] Grzybowski, B. A.; Whitesides, G. M. Three-Dimensional Dynamic Self-Assembly of Spinning Magnetic Disks: Vortex Crystals. *J. Phys. Chem. B* **2002**, *106*, 1188-1194.

[26] Grzybowski, B. A.; Fitzner, K.; Paczesny, J.; Granick, S. From dynamic self-assembly to networked chemical systems. *Chem. Soc. Rev.* **2017**, *46*, 5647-5678.

[27] Lee, T.; Gizynski, K.; Grzybowski, B. A. Non-Equilibrium Self-Assembly of Monocomponent and Multicomponent Tubular Structures in Rotating Fluids. *Adv. Mater.* **2017**, *29*, 1704274.

[28] Szpiro, G. G. *Kepler's conjecture*, Wiley, **2003**.

[29] Conway, J. H.; Sloane, N. J. A. *Sphere Packings, Lattices, and Groups*, Springer, New York, **1999**.

[30] COMSOL Multiphysics 5.1, COMSOL, Inc., Burlington, MA, USA.

[31] S. Strogatz, *Nonlinear Dynamics and Chaos*, CRC Press, Boca Raton, **2015**.

[32] Pampaloni, F.; Reynaud, E. G.; Stelzer, E. H. K. The Third Dimension Bridges the Gap between Cell Culture and Live Tissue. *Nat. Rev. Mol. Cell Biol.* **2007**, *8*, 839-845.

[33] Gracias, D. H.; Tien, J.; Breen, T. L.; Hsu, C.; Whitesides, G. M. Forming Electrical Networks in Three Dimensions by Self-Assembly. *Science* **2000**, *289*, 1170-1172.

[34] Leong, T. G.; Lester, P. A.; Koh, T. L.; Call, E. K.; Gracias, D. H. Surface Tension-Driven Self-Folding Polyhedra. *Langmuir* **2007**, *23*, 8747-8751.

Appendix

A.1 Transient structures and disordered assemblies.

For n = 8, polymorphs were also observed, but they are transient; the structures are transformed into the stable, symmetric structure within a few seconds (Figure A1a). As complexity of the components increases, i.e., the particles are non-identical and its shape is polygonal or rod-like or others rather than sphere, glassy packing is highly dominant (Figure A1b–d).

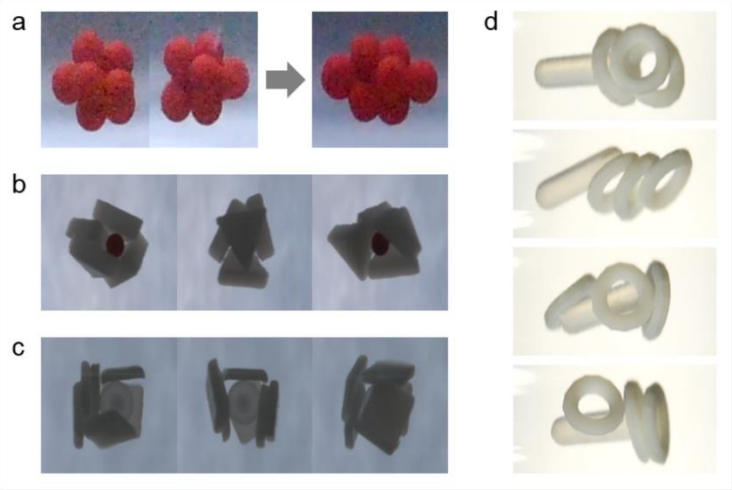

Figure A1. Transient structures for n = 8 and failure modes of ordered assemblies. a) For n = 8, transiently formed structures (left side of the arrow) spontaneously evolve into the stable, more symmetric packing shown on the right. Some examples of disordered assemblies for b) tetrahedral and c) hexahedral "cages", and d) an interlocked, "rotaxane" structure.

A.2 Evidence for the lack of hysteresis in Hopf bifurcation

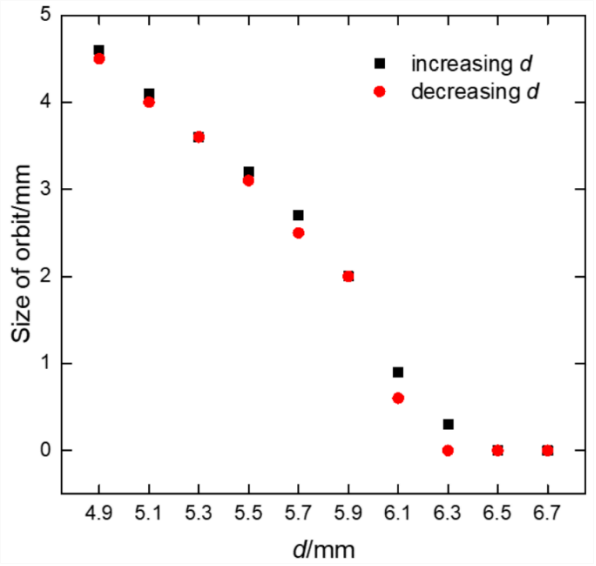

Figure A2. Changes in the particle's ring orbit upon decreasing and then increasing the value of parameter *d*. As the system transitions from a stable point to a limit cycle and then backwards, no hysteresis is observed. Experimental conditions are the same as in the main-text Figure 6h.

A.3 Estimation of the lower size limit of trapped particles

Even for the symmetrical case when both damped aluminum disks rotate at the same ω_1, the Navier-Stokes equations for the system cannot be solved analytically (*1*, *2*). Accordingly, we develop a semi-analytical model to estimate the lower size limit of trapped particles—we do so by linearizing the numerically calculated flow near the trap's center and by approximating the dependence of this linearization on relevant physical parameters. Justification of this approximation is given in section A.3.1 and is mostly based on fitting certain expressions to the numerical (FEM CFD) solutions of hydrodynamic equations. Thus obtained analytical expression of approximate flow is then used in sections A.3.2–A.3.3 to investigate the stability and fluctuations of small particles near the trap's center, with focus primarily on deriving a lower bound on the sizes of particles that can be trapped/confined.

A.3.1. Flow field near trap's center.

We show that flow field near the center of the trap can be linearized and, furthermore, that flow velocities in axial (U_z) and radial (U_r) directions are decoupled:

$$\begin{aligned} U_z &= -z(A_z + B_z r^2) \\ U_r &= A_r r \end{aligned} \qquad (1)$$

Furthermore, in the region where r is small enough such that the term $B_z r^2$ can be neglected, A_r and A_z must be related by $A_z = 2A_r$. This relation comes from the condition that near the trap's center, the net axial inflow must be equal to the net radial outflow—in other words, the divergence $\nabla \cdot \boldsymbol{U}$ of the flow must be zero. Taking the divergence of the flow (1) in cylindrical coordinates and neglecting $B_z r^2$ gives

$$0 = \nabla \cdot \boldsymbol{U} = \frac{1}{r} \cdot \frac{\partial (r U_r)}{\partial r} + \frac{\partial U_z}{\partial z} = \frac{1}{r} \cdot \frac{\partial (A_r r^2)}{\partial r} - A_z = 2A_r - A_z$$

which means that $A_z = 2A_r$.

We illustrate the applicability of this approximation by fitting analytical flow-field expression (1) to the results of FEM CFD at different experimental parameters. Figure A3a-d illustrates such fitting (in a small region of $0 < r < 1$ mm and -2 mm $< z < 2$ mm) against numerically computed flow field for one set of physically realistic parameters. As seen, e.g., in Figure A3b, the proposed approximation is quite precise (note that all three fitted, black curves use the same values of A_z and B_z).

To study the dependence of constants A_z and A_r on physical parameters, we fitted (1) to numerically calculated flows for various angular velocities of the tube (ω), the aluminum disks (ω_1), as well as for different viscosities (η). Figure A3e shows that indeed, to a good approximation, $A_z = 2A_r$ and the values A_r/η plotted against $(\omega - \omega_1)/\omega$ fall on the same master curve (black), which can be approximated to second order of $(\omega - \omega_1)/\omega$ as

$$A_z = 2A_r = K\frac{\eta}{\rho_{\mathrm{L}} H^2 \omega}\left((\omega - \omega_1) + 3\frac{(\omega - \omega_1)^2}{\omega}\right) \qquad (2)$$

where H is the distance between the rotors, ρ_L is the liquid density, and K is the dimensionless parameter that probably depends on the geometric aspect ratio of H to the tube's diameter (D_{tube}). For aspect ratio $H/D_{\mathrm{tube}} = 3$, we found that $K \approx 69$. Group $\eta/\rho_{\mathrm{L}} H^2 \omega$ is the inverse of Reynolds number. We emphasize that expression (2) is not really derived, but is rather a heuristics stemming from dimensional analysis, inspection of some limiting cases, and fitting to numerically calculated flow fields. As evident from the Figure A3e, this approximation is more precise when rotors are rotating not much slower than the tube (i.e., $(\omega - \omega_1)/\omega \ll 1$) and becomes less accurate as rotors' angular velocity ω_1 approaches zero (i.e. $(\omega - \omega_1)/\omega \approx 1$).

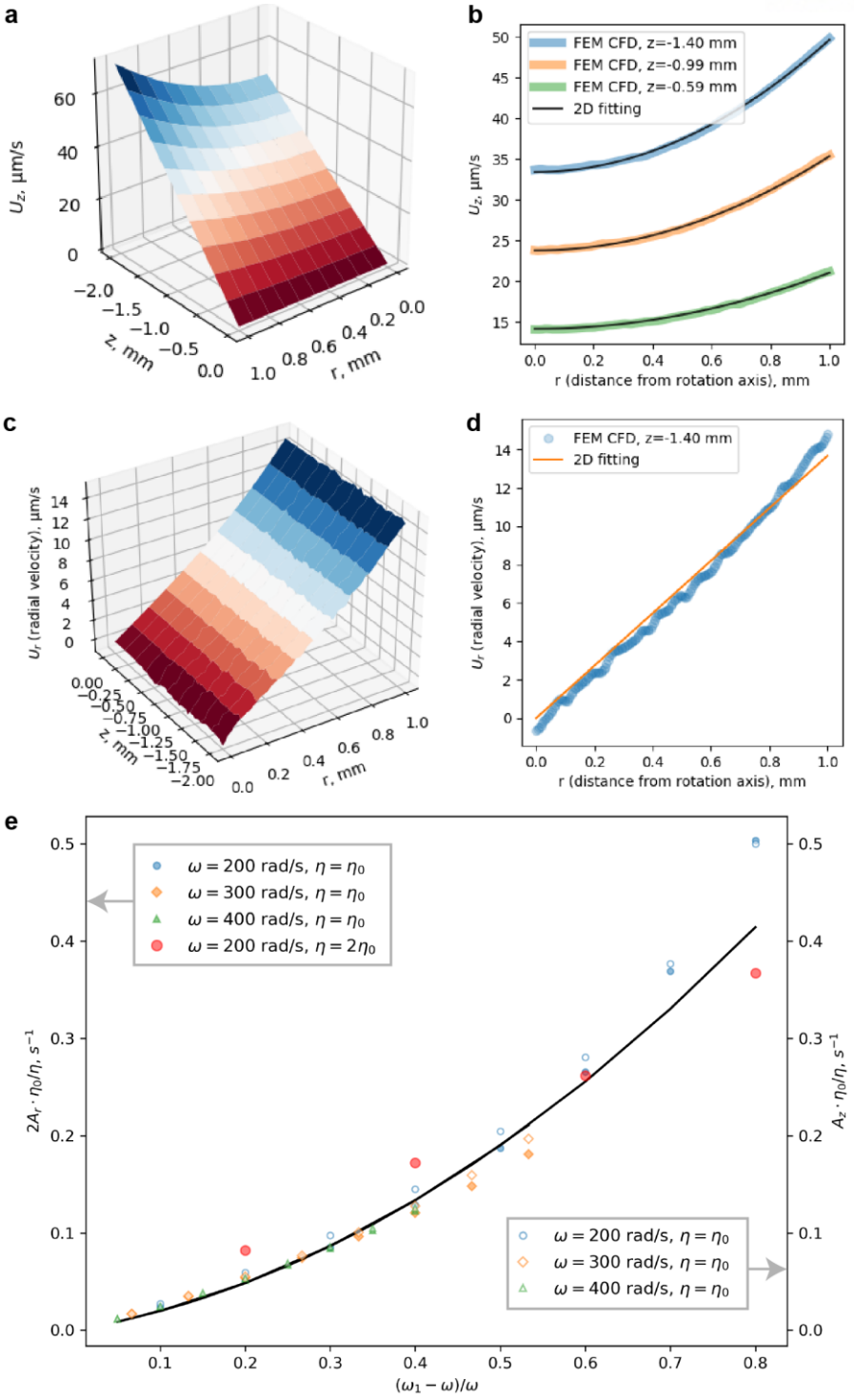

Figure A3. Analytical approximation of flow field in symmetric vortex trap compared to numerical FEM CDF calculations. a-d, Axial (a) and radial (c) components of the flow velocity computed numerically and plotted against radial (r) and axial (z) coordinates as 2D surface plots. Parameters used for this calculation are $D_{\text{tube}} = 10$ mm, $H = 30$ mm, $\omega = 200$ rad/s, $\omega_1 = 180$ rad/s, $\eta = 2.175$ mPa · s. b) Radial profiles of axial velocity at three different values of z (color curves)

compared to $U_z = -z(A_z + B_z r^2)$ traced by black curves. Values of A_z and B_z are the same for all three profiles. d) Radial profile of radial velocity fitted by $U_r = A_r r$. e) Fitting parameter $2A_r$ (filled markers), and fitting parameter A_z (empty markers), both scaled by viscosity η, are plotted against relative difference in angular velocities $(\omega - \omega_1)/\omega$. Black curve represents formula (2). Viscosity $\eta_0 = 2.175$ mPa · s.

A.3.2. Effective potential for a particle in the trap.

We will now derive the effective potential for small particle near the trap's center under the following assumptions:

1. Drag force on the particle is described by the Stokes formula: $\boldsymbol{F}_{\text{drag}} = 6\pi\eta R\boldsymbol{U}$, where η is the dynamic viscosity, R is the particle radius, U is the velocity of the flow relative to the particle.
2. Particle size is much smaller than the characteristic scales at which flow velocity changes, and the particle does not affect the flow at large. Specifically, velocity of the flow in the absence of the particle can be used as the value of velocity in the Stokes drag formula.
3. Particle size and its typical distance from the trap's center are small enough such that approximation (1) holds. Furthermore, particle's distance r from the rotation axis is small enough such that the term $B_z r^2$ can be neglected in (1).
4. Particle's angular velocity is matched to that of the fluid at particle's location, which is assumed to be constant near trap's center. This angular velocity is assumed to be equal to the tube's angular velocity ω.

Forces acting on a particle of radius R and density smaller by $\Delta\rho$ relative to the surrounding liquid are

$$F_r = -\frac{4}{3}\pi R^3 \Delta\rho \omega^2 r + 6\pi\eta R A_r r \tag{3a}$$

$$F_z = -6\pi\eta R A_z z \tag{3b}$$

The first term in (3a) is buoyancy due to centrifugal acceleration, $\omega^2 r$; the second term is Stokes' drag. It can be seen that these components for the force are proportional to displacements r and z along respective axes. Therefore, this trapping force can be seen as a manifestation of an effective potential

$$E = \frac{r^2}{2}\left(\frac{4}{3}\pi R^3 \Delta\rho \omega^2 - 6\pi\eta R A_r\right) + \frac{z^2}{2} 6\pi\eta R A_z \tag{4}$$

which is harmonic in each axis.

A.3.3. Lower limit on the size of particle that can be trapped and confined.

We will be saying that "particle can be trapped" if the particle attracts to the trap's center along both axes (r and z). It's easy to see that the axial force (3b) is always directed towards the trap's center. However, the radial force (3a) is directed towards the axis only if

$$-\frac{4}{3}\pi R^3 \Delta\rho\omega^2 + 6\pi\eta R A_r < 0$$

which can be expressed as a condition for the particle's radius

$$R > \frac{3}{\omega}\sqrt{\frac{\eta A_r}{2\Delta\rho}} \tag{5}$$

If this condition is not fulfilled, the particle will be radially repelled from the axis, not attracted to it. For example, condition (5) produces $R > 34\ \mu\text{m}$ for parameters $\omega = 200\ \text{rad/s}, \omega_1 = 40\ \text{rad/s}, \eta = 2.175\ \text{mPa}\cdot\text{s}, \rho_L = 1104\ \text{kg/m}^3, D_{\text{tube}} = 10\ \text{mm}$, $H = 30\ \text{mm}$. If we increase both ω and ω_1 fivefold in this example (this would correspond to $\omega = 10{,}000$ r.p.m.), value of A_r would remain the same, but smallest radius would decrease fivefold, to ca. 6 µm.

However, even if (5) is fulfilled and the particle is attracted to the trap's center along both axes, it is practically relevant to know how strongly the particle is kept at the trap's center. To quantify this property, we will be saying that "particle is confined" if the typical excursions of the particle from the trap center do not significantly exceed the particle's radius. This definition is not typical for other types of traps. In traps like optical tweezers and magneto-optical traps, potential well spans only a small region of space (blue curve in Figure A4b). Once the particle escapes the trap region by a fluctuation, it does not experience any attraction to the trap anymore and does not return, as illustrated by the orange trajectory in Figure A4b. The potential well depth is used to evaluate the time for which a particle can be trapped—the deeper the well (in relation to the thermal energy, $k_B T$), the longer it takes for a trapped particle to escape. In contrast, in our vortex-vortex trap, the potential well can span large part of the vessel volume (see basins of attraction in the main-text Figure 6i). However, in this case the trapping force near the center can be so weak that the magnitude of particle's Brownian motion in the trap exceeds particle's size: particle is "trapped", but not "confined" by our definitions.

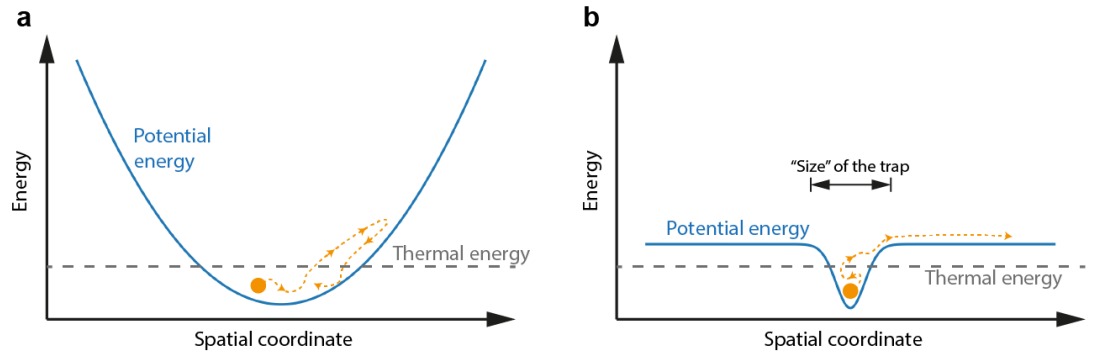

Figure A4. Difference between trapping potential in the vortex-vortex trap and other types of traps. a)

Potential in our vortex-vortex trap (blue) if parabolic and spans large part of the rotating tube's volume (see basins of attraction in the main-text Figure 6i). Thermal energy (dashed horizontal line) allows the particle (orange circle) to make excursions from the center (orange dashed line), possibly to distances larger than particle size, but the particle never leaves the trap's potential well. b) In other types of traps, potential well (blue) typically occupies only a small part of the vessel's volume, and once the particle (orange circle) leaves the well, it does not feel the returning force anymore.

Specifically, thermal fluctuations of particle position in potential (3) will lead to the Boltzmann distribution along each axis: probability densities for finding the particle at certain r and z locations are then given by

$$P(r) = P_{r=0} \exp\left(-\frac{\frac{r^2}{2}\left(\frac{4}{3}\pi R^3 \Delta\rho\omega^2 - 6\pi\eta R A_r\right)}{k_B T} \right) \tag{6a}$$

$$P(z) = P_{z=0} \exp\left(-\frac{\frac{z^2}{2} 6\pi\eta R A_z}{k_B T} \right) \tag{6b}$$

where $P_{r=0}$ and $P_{z=0}$ are the probability densities at $r = 0$ and $z = 0$, respectively, and can be found from normalization conditions $\int_0^\infty P(r)dr = 1$ and $\int_{-\infty}^\infty P(z)dz = 1$; T is the temperature, k_B is the Boltzmann constant. It is natural to define a particle as "confined" along a given coordinate if characteristic length of decay of the corresponding Boltzmann's distribution is smaller than the radius of the particle: $P(r = R) < P_{r=0}/e$ for radial direction, and $P(z = R) < P_{z=0}/e$ for axial direction. This condition means that the expression in the exponent's brackets in (6a) and (6b) must be less than -1 at $r = R$ and $z = R$, respectively:

$$-\frac{\frac{R^2}{2}\left(\frac{4}{3}\pi R^3 \Delta\rho\omega^2 - 6\pi\eta R A_r\right)}{k_B T} < -1 \tag{7a}$$

$$-\frac{\frac{R^2}{2} 6\pi\eta R A_z}{k_B T} < -1 \tag{7b}$$

These two conditions can be viewed as conditions on particle's radius. Condition for axial confinement (7b) can be written in a closed form

$$R^3 > \frac{k_B T}{3\pi\eta A_z} \tag{8}$$

Condition for radial confinement is a fifth-order polynomial inequality with respect to R, and should be solved numerically:

$$R^5 \cdot \left(\frac{2}{3} \cdot \frac{\pi\omega^2\Delta\rho}{k_B T}\right) - R^3 \cdot \left(\frac{3\pi\eta A_r}{k_B T}\right) > 1 \qquad (9)$$

Note that if this inequality is fulfilled, inequality (5) is also fulfilled.

The function $f(R) = \alpha R^5 - \beta R^3$ for $\alpha > 0$, $\beta > 0$, $R > 0$ has only one extremum at $R_{\min} = \sqrt{3\beta/5\alpha}$. This extremum is always a minimum and $f(R_{\min}) < 0$. At $R > R_{\min}$, the function $f(R)$ grows monotonically (Figure A5a shows $f(R)$ for $\alpha = 1$, $\beta = 1$). Therefore, equation $f(R) = 1$ has only one root R_0. Behavior of R_0 for different values of α and β is illustrated in Figure A5b. The limit of $\alpha \gg \beta$, which can also be expressed as $\omega^2\Delta\rho \gg \eta A_r$, corresponds to buoyancy force (due to centrifugation) dominating the drag forces. At this limit, the minimal radius will be defined by

$$R^5 > \frac{3k_B T}{2\pi\omega^2\Delta\rho} \qquad (10)$$

At the opposite limit $\alpha \gg \beta$, equivalent to $\omega^2\Delta\rho \ll \eta A_r$, condition of minimal radius becomes roughly equivalent to the condition (5) required for the radial force to be attractive.

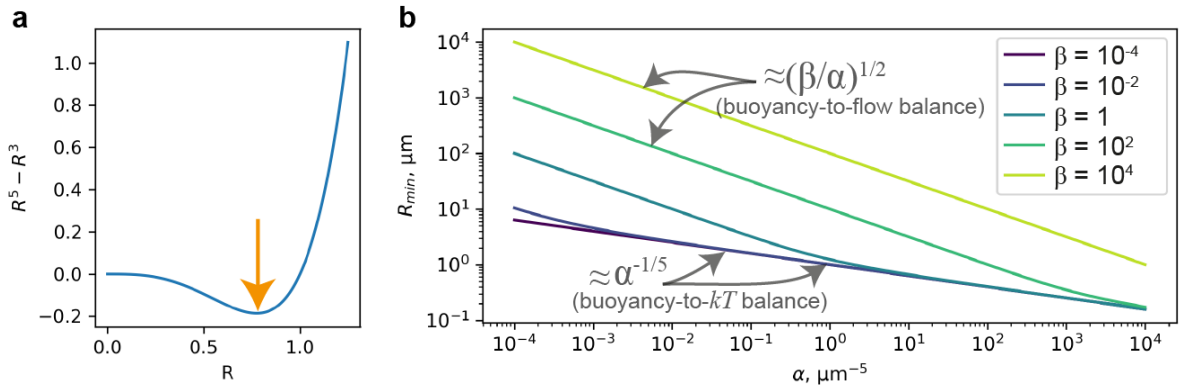

Figure A5. Analysis of radial confinement condition. a) Function $f(R) = R^5 - R^3$ plotted against R. Minimum at $R = \sqrt{3/5}$ is marked by orange arrow. b) Positive root of the equation $\alpha R^5 - \beta R^3 = 1$ for different values of α and β. At $\alpha \gg \beta$ limit, the root approaches $R \approx \alpha^{-5}$. At the opposite limit $\alpha \ll \beta$, root becomes approximately $R \approx (\beta/\alpha)^{1/2}$.

To sum up, trapping the particle requires only condition (5). Making axial displacements of the particle comparable to its radius requires condition (8). Making radial displacements of already trapped particle smaller than the radius happens automatically if $\omega^2\Delta\rho \gg \eta A_r$, requires condition (10) in the opposite limit, or should be found by solving fifth order polynomial inequality (9) if neither limit is applicable. In all these cases, analytical approximation (2) can be used for A_r and A_z. For example, particles with radius 34 μm can be trapped using parameters $\omega = 200\ \mathrm{rad/s}, \omega_1 = 40\ \mathrm{rad/s}, \eta = 2.175\ \mathrm{mPa \cdot s}, \rho_L = 1104\ \mathrm{kg/m^3}, D_{\mathrm{tube}} = 10\ \mathrm{mm}$, $H = 30\ \mathrm{mm}$, as mentioned above.

Particles of this radius will be axially confined (in fact, threshold radius for axial confinement is only 0.8 μm at these conditions), and radially confined (since $\omega^2 \Delta\rho \ll \eta A_r$ in this case; the threshold radius for radial confinement is 22 μm).

A.4 Appendix references

[1] Brøns, M.; Voigt, L. K.; Sørensen, J. N. Topology of Vortex Breakdown Bubbles in a Cylinder with a Rotating Bottom and a Free Surface. *J. Fluid Mech.* **2001**, *428*, 133-148.

[2] Lopez, J. M.; Marques, F. Mode Competition between Rotating Waves in a Swirling Flow with Reflection Symmetry. *J. Fluid Mech.* **2004**, *507*, 265-288.

License for reusing the published paper (1/2)

JOHN WILEY AND SONS LICENSE
TERMS AND CONDITIONS

Nov 10, 2019

This Agreement between Ulsan National Institute of Science and Technology ("You") and John Wiley and Sons ("John Wiley and Sons") consists of your license details and the terms and conditions provided by John Wiley and Sons and Copyright Clearance Center.

License Number	4705290925380
License date	Nov 10, 2019
Licensed Content Publisher	John Wiley and Sons
Licensed Content Publication	Advanced Materials
Licensed Content Title	Dynamic Assembly of Small Parts in Vortex–Vortex Traps Established within a Rotating Fluid
Licensed Content Author	Bartosz A. Grzybowski, Olgierd Cybulski, Yaroslav I. Sobolev, et al
Licensed Content Date	Jul 1, 2019
Licensed Content Volume	31
Licensed Content Issue	32
Licensed Content Pages	8

License for reusing the published paper (2/2)

Type of use	Dissertation/Thesis
Requestor type	Author of this Wiley article
Format	Print and electronic
Portion	Full article
Will you be translating?	No
Title of your thesis / dissertation	Dynamic Self-Assembly and 3D Fluidic Trap in Rotating Fluids
Expected completion date	Dec 2019
Expected size (number of pages)	80
Requestor Location	Ulsan National Institute of Science and Technology 50, UNIST-gil Ulsan 44919, Republic of Korea Ulsan, Ulsan 44919 Korea, Republic Of Attn: Ulsan National Institute of Science and Technology
Publisher Tax ID	EU826007151
Total	0.00 USD

Terms and Conditions

TERMS AND CONDITIONS

This copyrighted material is owned by or exclusively licensed to John Wiley & Sons, Inc. or one of its group companies (each a"Wiley Company") or handled on behalf of a society with which a Wiley Company has exclusive publishing rights in relation to a particular work (collectively "WILEY"). By clicking "accept" in connection with completing this licensing transaction, you agree that the

Summary (in Korean)

Acknowledgement (in Korean)

It was a great honor for me to join Bartosz' group in 2015. I would like to thank my advisor, Bartosz A. Grzybowski for giving me a chance to study in good condition, much support and advice during my doctoral course. Bearing lessons that he gave in mind, I will keep trying to become a fully qualified "independent researcher". I also thank committee members (prof. Steve granick, prof. Oh-Hoon Kwon, prof. Hyuk Kyu Pak and prof. Yoon-Kyoung Cho) for examining my doctoral thesis, proposing good advice, and encouraging me. I couldn't get good achievements and excellent experiences without my colleagues, Konrad, Slava, and Olgierd. It was my lucky to have my friends, Marta and Witek and many good, warm words that they gave me.

7년 반이라는 시간 동안 기다리고 지지해준 사람들이 너무나 많습니다. 사랑하는 아내 연희, 그리고 우리 아이들 서진이, 서연이에게는 무엇으로도 표현할 수 없는 고마운 마음을 전합니다. 어머니, 아버지의 지속적인 관심, 장모님, 장인어른의 따뜻한 격려와 배려, 제가 마음 편히 공부할 수 있었던 이유입니다. 형들, 처형네 가족에게도 감사하다는 말을 하고 싶습니다. 힘들 때 많은 위로와 공감을 해주었던 전윤남 박사, 박성준 박사, 그리고 장현숙 박사에게도 감사의 말을 전합니다. 마지막으로 같은 연구실 동료이자 친한 형 동생처럼 서로 의지했던 윤석민 박사, 정용광 박사, 준혁이, 은영이, 남훈이, 민주에게 고맙다는 말을 하고 싶습니다.

Curriculum Vitae

PERSONAL

Name	Taehoon Lee
Work address	50 Unist-gil, Ulju-gun, Ulsan 44919, Republic of Korea
Date of birth	Sep.5.1980
Nationality	Republic of Korea

EDUCATION

Ulsan National Institute of Science and Technology — Ulsan, Republic of Korea
Ph.D candidate in Physical Chemistry — September 2015 – Present
Advisor: Bartosz A. Grzybowski
Thesis title: "Dynamic Self-Assembly and 3D Fluidic Trap in Rotating Fluids"

Korea Advanced Institute of Science and Technology — Daejeon, Republic of Korea
Master of Science in Nuclear and Quantum Engineering — September 2012 – August 2014
Advisor: Sung-Min Choi
Thesis title: "SANS and SAXS Study of Packing Behavior of 1D Nanoparticles in Hexagonal Micellar Phase of Non-Ionic Surfactant System Depending on Diameter Ratio and Concentration"

Ajou University — Suwon, Republic of Korea
Bachelor of Science in Mechanical Engineering — August 2006

OTHER EXPERIENCES

Neutron Scattering and Nanoscale Materials Lab., KAIST, Researcher — Sep.2014 – Dec.2014
GM Korea, Small IP & Console Engineer — Sep.2010 – Aug.2012
LG Electronics, Mobile Phone Mechanical Engineer — Aug.2006 – Aug.2010

PUBLICATIONS

T. Lee, Y. I. Sobolev, O. Cybulski and B. A. Grzybowski, "Dynamic Assembly of Small Parts in Vortex-Vortex Traps Established within a Rotating Fluid", *Adv. Mater.* **31**, 1902298 (2019)

T. Lee, K. Gizynski, and B. A. Grzybowski, "Non-Equilibrium Self-Assembly of Monocomponent and Multicomponent Tubular Structures in Rotating Fluids", *Adv. Mater.* **29**, 1704274 (2017)

K. Gizynski, **T. Lee** and B. A. Grzybowski, “Dynamic Self-Assembly of Magnetic/Polymer Composites in Rotating Frames of Reference”, *Adv. Mater.* **29**, 1700614 (2017)

S.-H. Lim*, **T. Lee***, Y. Oh*, T. Narayanan, B. J. Sung and S.-H. Choi, “Hierarchically Self-Assembled Hexagonal, Honeycomb, and Kagome Superlattices of Binary 1D Colloids”, *Nat. Commun.* **8**, 360 (2017)

PRESENTATIONS

T. Lee, K. Gizynski, O. Cybulski, Y. I. Sobolev and B. A. Grzybowski, “Dynamic self-assembly of quasi-1D and 3D structures in rotating fluids”, ACS Spring 2019 National Meeting & Exposition, Orlando, USA, March 31- April 4, 2019

T. Lee, S-H Lim, T. Narayanan and S.-M. Choi, "Small-Angle Neutron and X-ray Scattering Investigation of Highly Ordered Binary 1D Nanoparticle Superlattice", 2015 International HANARO Symposium, Daejeon, Republic of Korea, May 11-15, 2015

T. Lee, S-H Lim and S.-M. Choi, "SANS and SAXS Investigation for Binary Superlattice of 1D Nanoparticles", 14th Korea-Japan Meeting on Neutron Science, Tokai, Japan, January 7-9, 2015

T. Lee, S-H Lim and S.-M. Choi, "Small-Angle Neutron and X-ray Scattering of Self-Assembled Binary Mixture of 1D Nanoparticles", 2014 HANARO Symposium, Daejeon, Republic of Korea, May 9, 2014